Shallow Radar (SHARAD), pedestal craters, and the lost Martian layers: Initial assessments

Daniel Cahn Nunes,[1] Suzanne E. Smrekar,[1] Brian Fisher,[2] Jeffrey J. Plaut,[1] John W. Holt,[3] James W. Head,[4] Seth J. Kadish,[4] and Roger J. Phillips[5]

Received 6 July 2010; revised 16 December 2010; accepted 24 January 2011; published 19 April 2011.

[1] Since their discovery, Martian pedestal craters have been interpreted as remnants of layers that were once regionally extensive but have since been mostly removed. Pedestals span from subkilometer to hundreds of kilometers, but their thickness is less than ~500 m. Except for a small equatorial concentration in the Medusae Fossae Formation, the nearly exclusive occurrence of pedestal craters in the middle and high latitudes of Mars has led to the suspicion that the lost units bore a significant fraction of volatiles, such as water ice. Recent morphological characterizations of pedestal deposits have further supported this view. Here we employ radar soundings obtained by the Shallow Radar (SHARAD) to investigate the volumes of a subset of the pedestal population, in concert with high-resolution imagery to assist our interpretations. From the analysis of 97 pedestal craters we find that large pedestals (diameter >30 km) are relatively transparent to radar in their majority, with SHARAD being able to detect the base of the pedestal deposits, and possess an average dielectric permittivity of 4 ± 0.5. In one of the cases of large pedestals in Malea Planum, layering is detected both in SHARAD data and in high-resolution imagery of the pedestal margins. We find that clutter is a major issue in the analysis of radar soundings for smaller pedestals, and tentative detection of the basal reflection occurs in only a few of the cases examined. These detections yield a higher average permittivity of ~6. The permittivity value derived for the larger pedestals, for which a basal reflection is unambiguous, is higher than that of pure water ice but lower than that of most silicate materials. A mixture of ice and silicates or an ice-free porous silicate matrix can explain a permittivity of ~4, and radar alone cannot resolve this nonuniqueness. Data from the Compact Reconnaissance Imaging Spectrometer (CRISM) tentatively confirms a mafic component in at least one pedestal in Malea Planum. Interpretation of SHARAD results can support either a mixture of ice and silicates or a porous silicate. The former is compatible with a model where nonpolar ice is periodically deposited in the midlatitudes as a result of obliquity variations. The latter is compatible with ash deposits, at least in where pedestals appear in volcanic centers such as Malea Planum.

Citation: Nunes, D. C., S. E. Smrekar, B. Fisher, J. J. Plaut, J. W. Holt, J. W. Head, S. J. Kadish, and R. J. Phillips (2011), Shallow Radar (SHARAD), pedestal craters, and the lost Martian layers: Initial assessments, *J. Geophys. Res.*, *116*, E04006, doi:10.1029/2010JE003690.

1. Introduction

[2] Evidence for environmental change on Mars over its geologic history began accumulating since the early days of planetary exploration. The two most prominent lines of initial observations entailed the various surface morphologies generated by ancient fluvial activity, valley networks and outflow channels [*Carr et al.*, 1977; *Carr*, 1979; *Sharp and Malin*, 1975], and the intricate layering seen at the polar layered deposits (PLD) [*Murray et al.*, 1972]. Collectively, these features span most of the history of the planet, with the networks in the Noachian and the PLD in the Amazonian; both are different expressions of the water cycle that reflect the prevailing environmental conditions of their respective times. Overall, Mars has clearly transitioned from a wet climate to a much drier one. Though the presence of phyllosilicate minerals [*McKeown et al.*, 2009] and evolved valley-network complexes [*Craddock and Howard*, 2002] in the Noachian highlands tend to support a past warm climate, these lines of evidence can also be partly explained through colder or

[1]Jet Propulsion Laboratory, California Institute of Technology, Pasadena, California, USA.
[2]Division of Engineering, Brown University, Providence, Rhode Island, USA.
[3]University of Texas at Austin Institute for Geophysics, Austin, Texas, USA.
[4]Department of Geological Sciences, Brown University, Providence, Rhode Island, USA.
[5]Planetary Sciences, Southwest Research Institute, Boulder, Colorado, USA.

Copyright 2011 by the American Geophysical Union.
0148-0227/11/2010JE003690

temperature-independent processes [e.g., *Fassett and Head*, 2008; *McKeown et al.*, 2009]. Even more recently in Martian history, in the late Amazonian, the rate of deposition in Planum Boreum may have noticeably increased, as trough migration paths are steeper near the surface [see *Smith and Holt*, 2010, Figure 2]. Also in the Amazonian, the distribution of surface water ice appears to have transitioned from a much more equatorward distribution to one increasingly polar [e.g., *Head et al.*, 2003]. Different geologic features have been used to support this idea. Lobate debris aprons (LDAs), for example, bear surface markings strongly suggestive of solid-state flow [e.g., *Carr and Schaber*, 1977] and are made almost entirely out of water ice [*Holt et al.*, 2008; *Plaut et al.*, 2009]. LDAs concentrate in areas where steep slopes are present in the midlatitudes [e.g., *Squyres*, 1979]. Fresh small craters, imaged soon after their formation, have also exposed what is likely to be clean water ice in the shallow subsurface at the midlatitudes [*Byrne et al.*, 2009]. The presence of clean ice tens of centimeters beneath the surface cannot be explained simply by atmospheric diffusion under current conditions. Though other processes need to be invoked, such as burial of snow or thermal contraction of pore ice, it is not presently clear what mechanism has led to these shallow ice deposits. Pedestal craters also are abundant throughout the midlatitudes and are thought to be the remnants of ancient layers that have since been mostly eroded [*McCauley*, 1973]. Some models have proposed that those layers were ice-rich and created during a period of higher obliquity [e.g., *Kadish and Barlow*, 2006]. If so, the material preserved in pedestals should also be ice-rich, but there has been no direct observational evidence of this composition until now.

[3] Pedestal craters were one of the new types of crater morphologies, distinct from craters seen previously on the Moon, discovered in the television data taken by Mariner 9 of the Martian midlatitudes and equatorial latitudes [*McCauley*, 1973]. They were initially described as craters located atop raised pedestals that are bound by relatively steep and serrated scarps and are approximately twice as wide as their respective central craters [*McCauley*, 1973]. A broader analysis of that data set revealed those craters to be concentrated in the midlatitudes, having diameters as small as subkilometer to as large as ~20 km, and with their pedestals tending to be azimuthally symmetric and spanning as wide as the outer portions of ejecta blankets around lunar craters of similar scaling [*Head and Roth*, 1976]. *Arvidson et al.* [1976] noted a possible correlation between pedestal craters and midlatitudinal mantle units [*Soderblom et al.*, 1973], and that pedestals tend to be wider and thicker with increasing latitude. The formation models that arose from those observations invoked erosion to explain how pedestals became elevated with respect to their surroundings, but they differed among themselves by the particular mechanisms giving the pedestals their shape. *McCauley* [1973] postulated that pedestal craters represent the action of wind erosion, where the plains surface deflated by at least as much as the thickness of the pedestals and the impact ejecta in each of those craters acted as an armor or lag deposit to protect the underlying material from removal. *Arvidson et al.* [1976] suggested that secondary cratering and pitting of the area surrounding a crater elevate the wind drag velocity threshold for erosion to prohibitively high values and protect the terrain surface, while leaving the pedestal perimetric scarp susceptible to eolian erosion. *Head and Roth* [1976], in contrast, argued that eolian erosion was not likely under prevailing winds because it would not maintain the observed azimuthal symmetry of pedestals, instead offering the hypothesis that the shape of pedestals are primarily controlled by the emplacement of the ejecta itself. *Mutch and Woronow* [1980], like *Head and Roth* [1976], hypothesized that pedestals are due primarily to emplacement processes, as the fresh appearance of the crater rims and azimuthal symmetry are not consistent with erosive mechanisms. Further, *Mutch and Woronow* [1980] concluded that pedestal craters did not reach the putative subsurface volatile reservoir during excavation, thus failing to have their ejecta fluidized.

[4] *Edgett et al.* [1997] examined pedestal craters in the area of the Medusae Fossae Formation. Based on their interaction with late stage (i.e., stratigraphically youngest at the location) lava flows and the superposition of different units, they concluded that the pedestal craters formed on a mantling layer of fine-grained material, older than the radar stealth unit of *Muhleman et al.* [1991] and *Muhleman et al.* [1995], that is likely of volcanic origin and deflated by wind. *Edgett et al.* [1997] especially noted cases where the stratigraphically youngest volcanic flows have been diverted by pedestals at a time when those pedestals had larger diameters, which suggests prolonged or ongoing erosion. *Kadish et al.* [2008] found pedestal craters in the tropical zone of Mars are exclusive to the Medusae Fossae Formation (MFF) [e.g., *Kadish et al.*, 2008; *Leuschen et al.*, 2003], and the geology of the area, dominated by volcanic flows and MFF friable deposits [*Edgett et al.*, 1997; *Scott and Tanaka*, 1986], is distinct from most of the other midlatitudinal areas, such as the different sedimentary members of the Vastitas Borealis Formation [*Skinner et al.*, 2006a; *Tanaka and Scott*, 1987], where the majority of pedestals occur. Still, the association between pedestal craters and mantle units gained strength with the high-resolution topography and imagery data obtained by the Mars Global Surveyor.

[5] *Tanaka and Kolb* [2001] mapped the Martian polar regions, including the different members of the Dorsa Argentea Formation (DAF), and established the age of the units from counting craters. They found the members of the DAF to be from the Early to Late Hesperian epoch and to consist of fine, unconsolidated material mantling the Noachian cratered highlands and underlying the Amazonian polar deposits. The cavi members of DAF possibly correspond to the explosive or discharge source region for a volatile-rich material of fine-grained texture, which was later eroded preferentially to produce pedestal and exhumed craters [*Tanaka and Kolb*, 2001]. In fact, a number of investigations of southern circumpolar area dating back to Mariner 9 had already proposed the removal of extensive, mechanically weak deposits [e.g., *Cutts*, 1973; *Murray et al.*, 1972], but they were limited in their analysis by the quality of the Mariner 9 data. *Plaut et al.* [1988] found similar evidence in the Viking orbital data set, which was of higher quality than that of Mariner 9. *Head and Pratt* [2001] interpreted the sinuous ridges in DAF as eskers and the cavi and sinuous channels as features related to the melting, collapse, and water flow from a paleounit, which they characterized as a broad, static glacial deposit. Although *Head and Pratt* [2001] briefly alluded to pedestal craters as remnants of the glacial deposit,

it was *Bleacher et al.* [2003] who presented topographic measurement of the pedestals to document extensive deflation of the DAF members.

[6] Between the latitudes of 30° and 60° in both hemispheres, *Mustard et al.* [2001] identified a surficial unit in Mars Orbiter Camera narrow-angle (MOC-NA) images that presents varying degrees of preservation. While intact portions appear to be smooth and of uniform thickness, between 1 and 10 m and mantling the underlying topography, the dissected portions contain pits and remnant ridges devoid of any layering and with a marked absence of mobile sediments. Based on morphology and thermal inertia properties, *Mustard et al.* [2001] concluded that this mantle layer consists of ice-cemented dust, possibly formed in the last high-obliquity period (~100–300 ka) when ice was stable at the surface globally and migrated from the poles equatorward [e.g., *Mellon and Jakosky*, 1995]. *Kreslavsky and Head* [2002] also concluded that the layered mantle at the middle to high latitudes consists of an ice-rich sedimentary deposit, but that such deposit has undergone a complex history of repeated deposition and removal in response to obliquity variations over time. *Head et al.* [2003] incorporated the estimated obliquity histories for Mars for the past 3 Myr [*Laskar et al.*, 2002] into global circulation models and determined that surface ice may have extended as far as 30° latitude between 0.4 and 2.1 Ma. Given that more recent orbital modeling by *Laskar et al.* [2004] indicates that over longer timescales (>250 Myr) average Martian obliquity was nearly twice as much as the current value of 25°, it is plausible that many more cycles of deposition and desiccation took place and that more extensive ice deposits once existed at the midlatitudes to equatorial latitudes. *Levrard et al.* [2004] offered that the direct deposition of ice at the high latitudes during low obliquities occurred in response to transitions from high obliquities and equatorial ice deposits.

[7] Recent mapping of pedestal craters using the latest high-resolution imagery by *Barlow* [2006] and *Kadish et al.* [2009] indicates that pedestals are more numerous in the northern than in the southern hemisphere and have a longitudinal preference for 60° to 180°E and 0° to 90°E, respectively, corresponding to regional clusters at Utopia, Acidalia, and Arcadia planitiae, and Malea Planum. Composing an equatorial cluster, the Medusae Fossae pedestal craters tend to be larger, less circular, and with broader pedestals than on the rest of the planet, while their morphology is commonly characterized by jagged edges and yardangs. In studying the crater population, *Kadish et al.* [2009] determined that the ratio (P/C) between pedestal and crater radii is larger for the northern hemisphere, with the pedestals extending farther from their parent craters than the ejecta seen around non-pedestal craters with single-layer ejecta [*Barlow*, 2006]. This finding implies the ejecta blankets, previously thought to be the mechanism responsible for armoring the surface of pedestals, do not generally extend as far out from their crater as the pedestals.

[8] Further evidence supporting the genetic link between volatile-rich units and pedestal craters is the finding of pits at the perimeter of some pedestals in both the southern and northern hemispheres. *Kadish et al.* [2008] found such pits for ~3% of the 2696 pedestals identified, this portion consisting of pedestals that are anomalously tall (~100 m, versus a population mean of ~50 m and range from 25 to 150 m [*Kadish et al.*, 2009]). These pits have a morphology that is similar to the sublimation pits seen in the swiss cheese terrain in the southern polar cap [e.g., *Thomas et al.*, 2000], and in some cases they merge to form moats around the pedestals. *Kadish et al.* [2008] concluded that sublimation of ice in the pedestal deposit creates these pits and that as sublimation progresses at the edge of the armored surface, a debris cover develops to smooth out the marginal slopes. The processes of pitting and debris covering at the margins theoretically reach a balance and act to stabilize the margins of pedestals.

[9] The evidence for volatile-rich pedestals, however, is indirect, as there is no information on the composition of the pedestal material. Because pedestals are possibly related to past or present reservoirs of water ice and may hold a record of climate change away from the polar regions, stronger evidence is sought. The Shallow Radar (SHARAD) aboard the Mars Reconnaissance Orbiter (MRO) is an instrument well suited to seek such evidence, as it has a vertical resolution of ~10 m and has identified other nonpolar ice reservoirs (lobate debris aprons, or LDAs [*Holt et al.*, 2008; *Plaut et al.*, 2009]). Here we present the results of the soundings performed by SHARAD on a small yet representative number of pedestal craters at the Martian midlatitudes, shown in Figure 1.

2. Observations

2.1. Instrument and Methodology

[10] The Agenzia Spaziale Italiana (ASI) provided SHARAD, a nadir-looking sounder, as a contributed instrument aboard NASA's Mars Reconnaissance Orbiter. The system consists of a linearly modulated chirped radar with a center frequency of 20 MHz, a bandwidth of 10 MHz, and a pulse duration of 85 μs, which translate into a wavelength and range resolution of 15 m in free space [*Seu et al.*, 2004]. The vertical resolution in the subsurface changes by a factor of $\sqrt{\varepsilon_0/\varepsilon}$, where ε is the permittivity of the medium (ε_0 is the permittivity of free space). From the MRO orbital altitude (~300 km [*Zurek and Smrekar*, 2007]), the cross-track resolution is bound by the diameter of the first Fresnel zone, 3 km, and the pulse-limited diameter, 6 km [*Seu et al.*, 2007]. The horizontal resolution along track is higher than cross track as a result of the synthetic aperture processing (SAR), and it ranges between 0.3 km and 1 km [*Seu et al.*, 2007].

[11] The overall population of pedestal craters has a mean crater diameter of 1.37 ± 0.57 km and a mean pedestal-to-crater ratio (P/C) of 3.09 ± 1.22, with uncertainties representing 1σ levels [*Kadish et al.*, 2009]; P/C reaches values beyond 6 in some rare cases, as in Medusae Fossae pedestals. Propagation of uncertainties for uncorrelated variables places the mean pedestal diameter at 4.23 ± 2.43 km, which is within the along-track resolution of SHARAD but only at the threshold of cross-track resolution. Consequently, roughly 84% (or smaller than the +1σ level) of the pedestal crater population is too small, compared to the Fresnel zone diameter, to be laterally resolved by SHARAD. In contrast, pedestal thicknesses, typically between 20 m and 80 m for the overall population as determined by *Kadish et al.* [2010], and between 20 and 60 m for the northern crater forms of *Skinner et al.* [2006b]. Such thickness values are greater than the vertical resolution of SHARAD, even assuming a low value of 2 for the permittivity of porous geologic materials

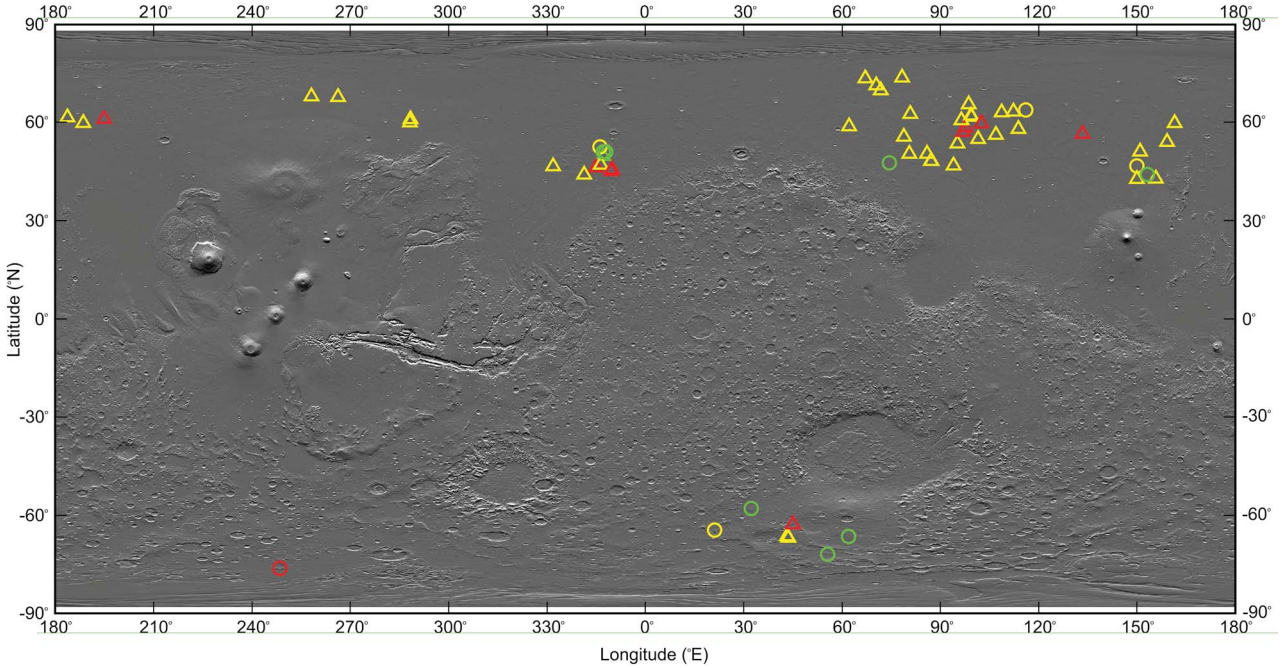

Figure 1. Locations of the pedestal craters examined in this study superimposed on MOLA shaded relief map. Triangles correspond to small pedestals (<30 km), while circles correspond to large (>30 km) pedestals. A green symbol signifies a positive detection, yellow a suspected but unconfirmed detection, and red a negative detection of subsurface reflectors beneath the pedestal surface.

(i.e., 10.6 m vertical resolution). We have therefore included in our survey pedestals that exceed 6 km in lateral dimensions, randomly selecting a total of 97 individuals across the areas of large pedestal concentrations (Acidalia, Arcadia, and Utopia Planitiae, Malea and Parva Plana).

[12] Radar reflections occur as a result of contrasts in the real component of the dielectric permittivity (ε') across interfaces that are sharp with respect to the wavelength of the SHARAD wave, such as that between the atmosphere and the surface or possibly that between two geologic layers [e.g., *Nunes and Phillips*, 2006; *Wait*, 1970; *Ward et al.*, 1968]. Attenuation of the signal occurs through either scattering, be it due to the roughness at interfaces or to heterogeneities in the volume of a medium, or through electric conductive losses, which depend on the imaginary component of the complex permittivity (ε') of materials and signal frequency [e.g., *Campbell*, 2002; *Daniels*, 2008; *Ulaby et al.*, 1986]. Both composition and porosity control the value of the real and the imaginary components of the complex permittivity; Table 1 summarizes plausible permittivity values at SHARAD frequencies and Martian temperatures for the materials relevant to this study. The real component generally ranges between 4.9 and 9.6 for bulk dry volcanic materials and is weakly dependent on signal frequency [e.g., *Ulaby et al.*, 1986]. The imaginary component (also given as the loss tangent, $\tan\delta = \varepsilon''/\varepsilon'$) for those same materials may vary by orders of magnitude, between 10^{-3} and 10^{-1}, according to the TiO+FeO content [*Olhoeft and Strangway*, 1975]. Electrically conductive or magnetic minerals, such as gray hematite, and minerals resulting from aqueous alteration of volcanic rocks, such as phyllosilicates, are inherently lossier because of their elevated ε'' values (>10^{-1}) [*Grimm and Stillman*, 2008; *Stillman and Olhoeft*, 2008], but evidence is lacking for their geographically widespread presence on the Martian surface [*Christensen et al.*, 2001; *Poulet et al.*, 2005]. Although not a compositional and mineralogical facsimile of the Martian regolith, the JSC Mars-1 Regolith Simulant [*Allen et al.*, 1997] is an often cited Martian analog; permittivity measurements by *Stillman and Olhoeft* [2008] at sounder frequencies (1–100 MHz), Martian temperatures (180–300 K), and soil-like densities (1600 kg m^{-3}) give $\varepsilon' = 2.84$ and $\tan\delta \leq 10^{-1}$. Extrapolation of these values to densities comparable to bulk rocks via the formulation for lunar regolith of *Olhoeft and Strangway* [1975] yields $\varepsilon' = 8.61$, which is closer to the upper limit given by *Ulaby et al.* [1986]. Water ice has lower overall permittivity values, with the complex permittivity sensitive to signal frequency and, especially, temperature. Whereas the real component varies only by a few percent for the range of temperatures found on Mars, the imaginary component spreads over several orders of magnitude.

[13] Several models exist to describe the dielectric behavior of water ice. *Nunes and Phillips* [2006] examined the models of *Chyba et al.* [1998] and *Matzler* [1998] for SHARAD frequencies and a temperature range from 150 K to 220 K and determined the following ranges: $3.08 \leq \varepsilon'_{ice} \leq 3.1$ and $10^{-9} \leq \varepsilon''_{ice} \leq 10^{-4}$. The constant value of $3.15 + i\,6.3 \times 10^{-4}$, as in

Table 1. Permittivities for SHARAD Frequencies and Martian Temperatures

Material	ε'	tan δ	Notes
H_2O ice	3.15	6.3×10^{-3}	
Mafic silicates	4.9 to 9.6	10^{-3} to 10^{-1}	
JSC Mars-1	2.84	$\leq 10^{-1}$	at 1600 kg m^{-3}
JSC Mars-1	8.61	$\leq 10^{-1}$	bulk[a]

[a]Corrected via the density relationship of *Olhoeft and Strangway* [1975].

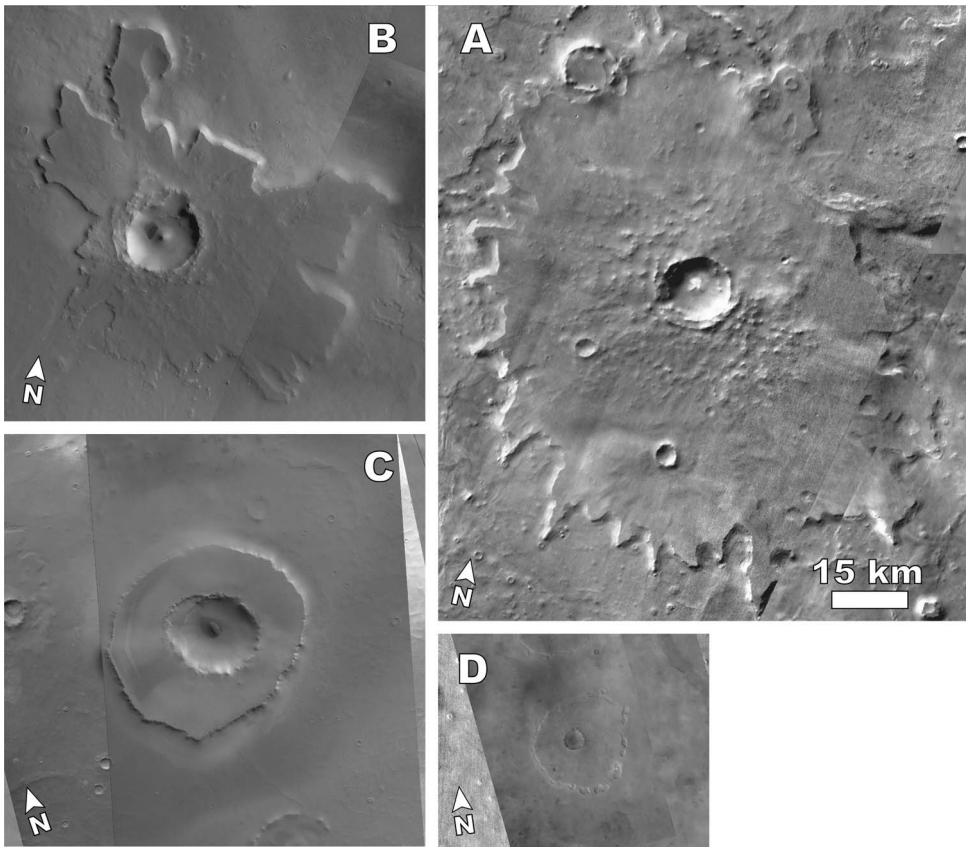

Figure 2. Four examples of pedestal craters of different sizes and morphologies, all drawn to the same scale. Figures 2a–2c extracted from the global daytime THEMIS-IR mosaic, while Figure 2d is a portion of CTX image P01_001555_2430_XN_63N260W. (a) Malea Planum, 66.37°S and 62.00°E. (b) Malea Planum, 71.73°S and 55.55°E. (c) Parva Planum, 76.06°S and 248.52°E. (d) Utopia Planitia, 62.38°N and 99.40°E. Scale bar and north arrow apply to all panels.

the work by *Picardi et al.* [2004], is a good representation for temperatures between 200 K and 230 K with respect to the models. *Pettinelli et al.* [2003] experimentally obtained a range of $2.89 \leq \varepsilon'_{ice} \leq 3.29$ and $\varepsilon''_{ice} \sim 6 \times 10^{-2}$ for 1 MHz and 250 K, depending on the method used. Here we adopt the same value as *Picardi et al.* [2004], which is not only in agreement with the values discussed above, but also is consistent with the observations of a low-loss, nearly pure ice northern polar layered deposits by both *Picardi et al.* [2005] and *Phillips et al.* [2008].

[14] One important issue when examining SHARAD radargrams is that the radar illuminates a broad swath of the actual Martian surface to each side of the spacecraft ground track. Off-nadir surface relief at a greater range than the surface at nadir can produce reflections, known as clutter, that arrive after the main surface (nadir) reflection and can overprint or be confused with returns from subsurface features [e.g., *Phillips et al.*, 1973]. To help distinguish clutter from possible subsurface reflections we employ the clutter model of *Holt et al.* [2006, 2008]. This model utilizes the gridded digital elevation model (DEM) derived from the Mars Orbiter Laser Altimeter (MOLA) [*Smith et al.*, 2001] data set along with spacecraft ancillary information to generate synthetic radargrams for each ground track of interest. All of the features seen in these synthetic radargrams correspond to surface echoes only, i.e., nadir and clutter, because the model input lacks any information about the subsurface. Since the model does not account for phase information and the signal is added incoherently, the synthetic radargrams, or cluttergrams, typically overestimate the amount and the intensity of clutter seen by SHARAD. Throughout our figures we overlay cluttergrams and the negative of their respective radargrams to help with the identification of subsurface reflections at pedestal craters (e.g., Figure 4).

2.2. Large (>30 km) Pedestals

[15] Although the equatorial population of pedestals in Medusae Fossae has the largest mean diameter according to *Kadish et al.* [2009], the largest individual pedestals occur in Malea Planum in the southern middle to high latitudes. Figures 2a and 2b show two of these anomalously large pedestals, each more than 50 km across and as much as ~115 km in the largest lateral dimension. Curiously, each of the three largest Malea pedestals has a very different planform shape from the others, perhaps due to different emplacement or erosional histories. Despite their gigantism, the height of these pedestals is comparable to that of much smaller pedestals around Mars (e.g., Figure 3). The MOLA PEDR profiles in Figure 3 for the pedestals in Figures 2a and 2d show a height of ~100 m above the surrounding terrain despite their diameters differing by a factor of ~6. This similarity in height suggests that the thickness of the pedestal

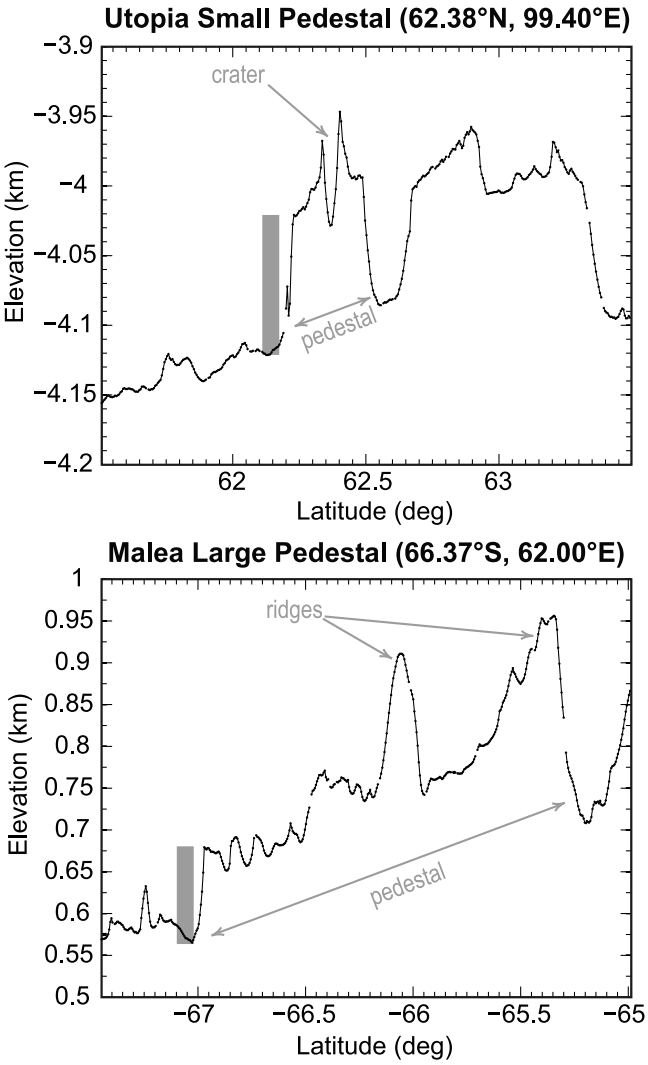

Figure 3. MOLA profiles of the pedestal craters in Figures 2a and 2d. Heights of the pedestals, marked by gray vertical bars, are comparable (~100 m) despite their greatly differing lateral scales.

may have more to do with the nature of the surface paleolayer, now largely deflated, than the size of the crater.

[16] The largest of the Malea Planum pedestals, centered at 66.37°S and 62.00°E (Figure 2a) and dubbed LMP1 here, is azimuthally asymmetric and is approximately 89 × 115 km. In contrast, the central crater is only 14.5 km in diameter, giving the feature a median P/C ratio of 7.04, which is more than twice the mean of 3.09 of the entire pedestal population. The perimeter of LMP1 is quite sinuous over length scales of 5 to 10 km, and the pedestal overlays some tectonic ridges associated with the caldera of Malea Patera. SHARAD coverage of LMP1 consists of more than 30 tracks that spread somewhat evenly across the pedestal domain, and it contains radargrams from regional surveys as well as radargrams specifically targeted at the pedestal. The radargrams are equally split between day and nighttime data acquisitions, the latter being generally of degraded quality because of defocusing effects imparted by the dayside ionosphere [*Seu et al.*, 2007]. A time domain radargram for LMP1 is shown in Figure 4 along with the clutter simulation ("cluttergram") and the ground track superposed on the MOLA DEM. Where the surface of the pedestal is flat (SW or right side of the frame), the first reflection is sharp and strong, suggesting a relatively smooth surface at scales comparable to the radar wavelength (15 m). Multiple weaker echoes follow the surface reflection in this area, each with a progressively larger delay (i.e., depth)

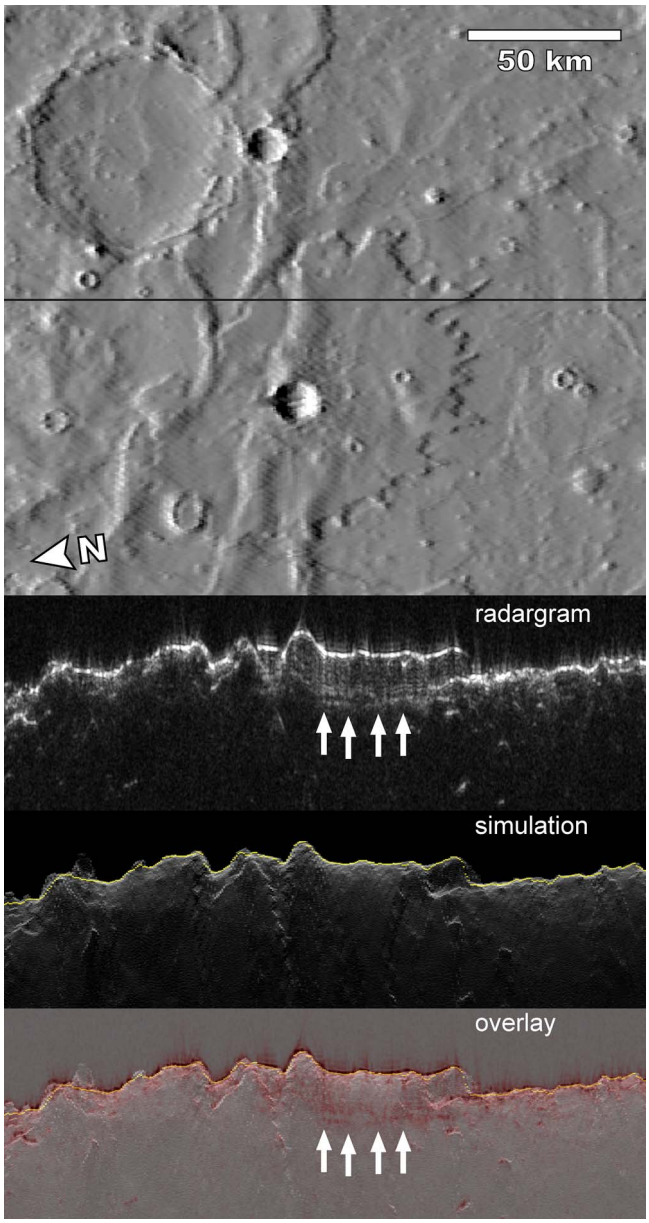

Figure 4. Example of SHARAD sounding of a large pedestal in Malea Planum (in Figure 2a). Multiple echoes are seen to occur after the surface reflection at the pedestal deposit, which have no counterparts in the clutter simulation and a consequent due to subsurface reflectors. From the top downward are the MOLA elevation data with the SHARAD ground track, radargram 748401, clutter simulation for 748401, and overlay of cluttergram and the inverted radargram in red. Arrows point to the latest (lowest) echo observed at the pedestal. Radargram and cluttergram are in time domain.

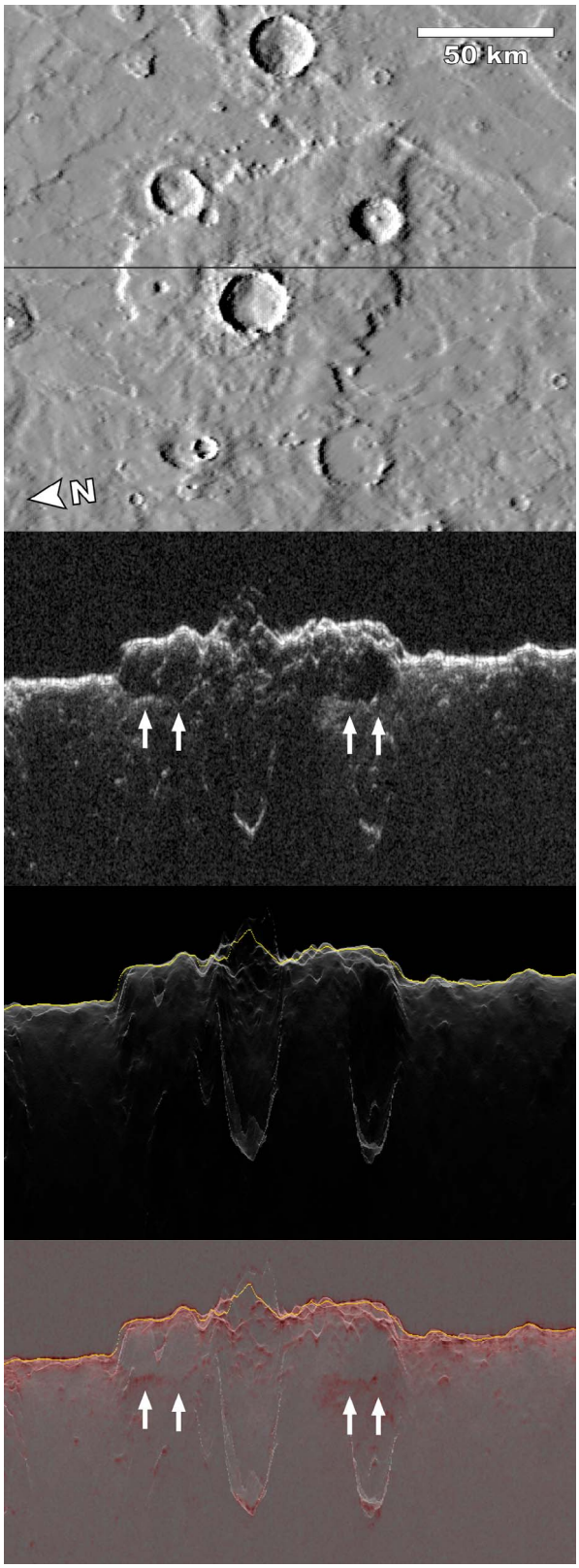

Figure 5. SHARAD radargram 782801 of a large pedestal (57.86°S, 32.56°E) in Malea Planum with the accompanying MOLA DEM, ground track, and clutter simulation, as in Figure 4. White arrows denote features in the radargram that do not have equivalents in the cluttergram and therefore correspond to subsurface reflections.

than the previous. Clutter simulation based on the MOLA DEM does not reproduce this sequence of weak echoes and confirms their subsurface nature. SHARAD data therefore indicate that LMP1 is layered, at least in the dielectric sense. The lowermost of the echoes in this sequence, marked by arrows in Figure 4, is delayed by ~1.9 μs and 8 to 10 dB weaker with respect to the surface reflection, and we interpret it to be the reflection generated at the basal interface between the pedestal and the underlying surface (Late Noachian to Early Hesperian, [*Leonard and Tanaka*, 2001]; Noachian, *Williams et al.* [2009]). The intermediate echoes are weaker in power than the basal reflection, possibly suggesting a lesser dielectric contrast between the internal layers than at the basal interface. All of the subsurface reflections in this portion of the pedestal follow the surface topography over the central ridge, disappearing or merging with clutter to the NE (left) of the ridge. These characteristics are present in most of the radargrams of this pedestal, although variations in power occur for the subsurface reflections; internal layering is not visible above the noise level in some cases, and between 8 and 10 layers are seen in the better cases.

[17] The second largest pedestal in Malea Planum (57.86°S, 32.56°E, dubbed LMP2 here) also presents relatively strong subsurface reflections. LMP2 has the approximate planform shape of an arrowhead, 140 × 95 km, appearing to derive from the combined effect of two of craters 11 and 15 km in diameter (Figure 5). Though the maximum P/C ratio is 9.3, the more likely value is 6.3 because the largest dimension appears to be the combined effect of the two craters. The pedestal perimeter is sinuous at length scales <10 km and delineated by well-defined scarps (as opposed to gently grading into the surrounding terrain). LMP2 is highest at its central portions, approximately 130 m, and shorter at its western and eastern extremities; the SHARAD radargram in Figure 5 traverses the pedestal at its tallest, central section. A comparison between the radargram and the MOLA-predicted cluttergram shows that the late reflections occurring to the north and south sides of the crater correspond to a subsurface interface between 2.75 μs and 3.75 μs and approximately 10 dB weaker with respect to the surface reflections. We interpret these two reflections as the contact between the pedestal deposit and the underlying Noachian and Hesperian surfaces [e.g., *Tanaka and Scott*, 1987; *Williams et al.*, 2009]. All of the 19 radargrams covering this pedestal fail to show any internal layering between the surface and basal reflections above the noise floor.

[18] The third large pedestal crater in Malea Planum (71.73°S, 55.55°E, dubbed LMP3 here), Figures 2b and 6, shows a much less symmetric shape, suggesting it has either undergone a greater degree of erosion or possibly derived from an oblique impact [e.g., *Herrick and Hessen*, 2006]. Another distinctive characteristic of LMP3 is the pronounced slope of its pedestal surface, with the northern and southern margins standing as high as ~300 m and between 0 and 100 m above the surrounding terrain, respectively. This slope does not reflect the local slope of the surrounding terrain and may be due to either a nonuniform thickness of the pedestal deposit or differential erosion. At its largest dimension (NW-SE), LMP3 spans ~80 km, in contrast to ~45 km in the north-south direction. The central crater is 14 km in diameter, giving a maximum pedestal to crater ratio of 5.7. The radar signature at LMP3 is more difficult to interpret. The radar-

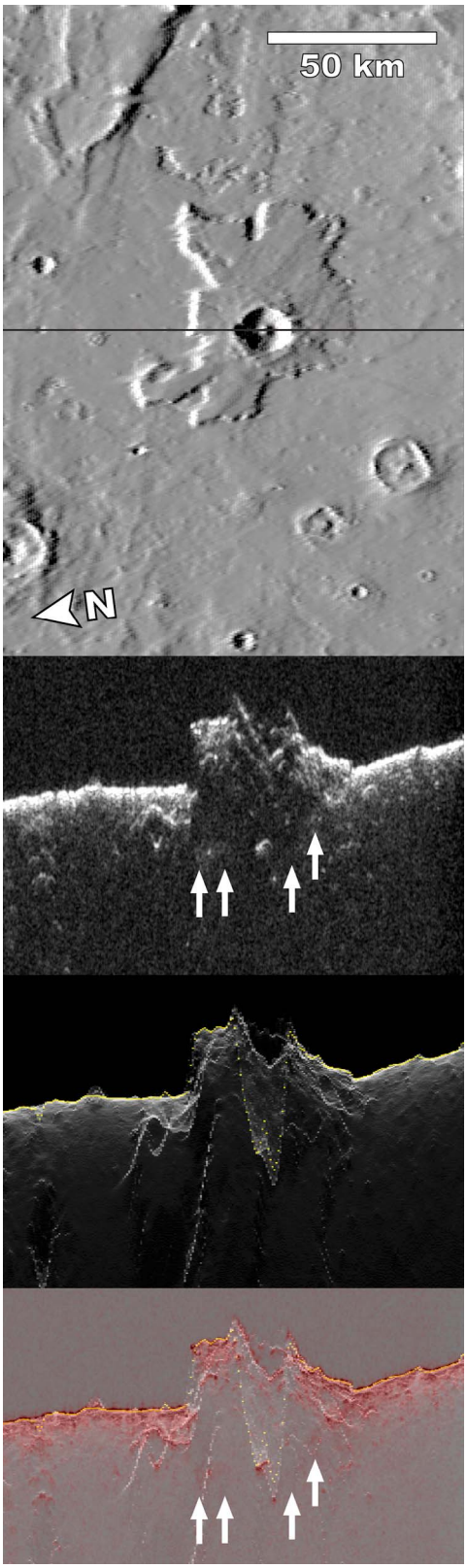

Figure 6. SHARAD radargram 797201 of a large pedestal (71.73°S, 55.55°E) in Malea Planum with the accompanying MOLA DEM, ground track, and clutter simulation. White arrows denote features in the radargram that do not have equivalents in the cluttergram and therefore correspond to subsurface reflections.

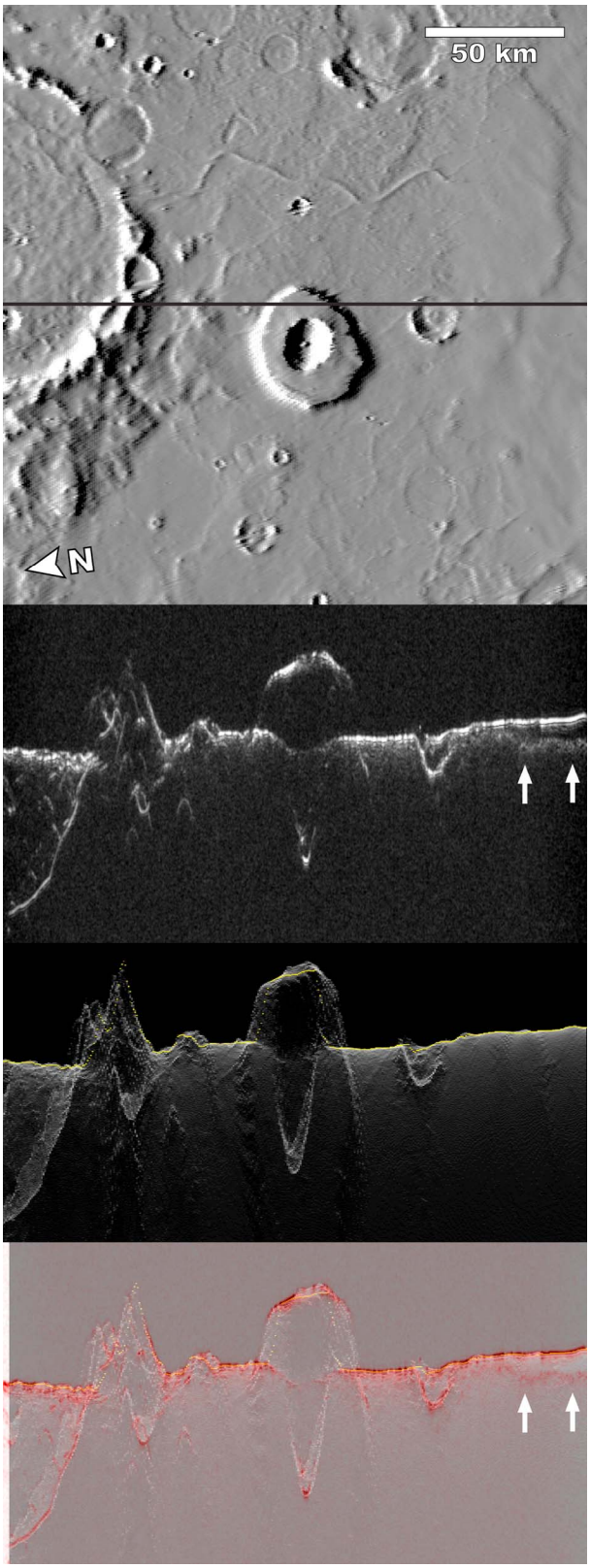

Figure 7. SHARAD radargram 905901 of the large pedestal (76.06°S 248.35°E) in Parva Planum with the accompanying MOLA DEM, ground track, and clutter simulation. Although not associated with the pedestal, white arrows denote features in the radargram that do not have equivalents in the cluttergram and therefore correspond to subsurface reflections.

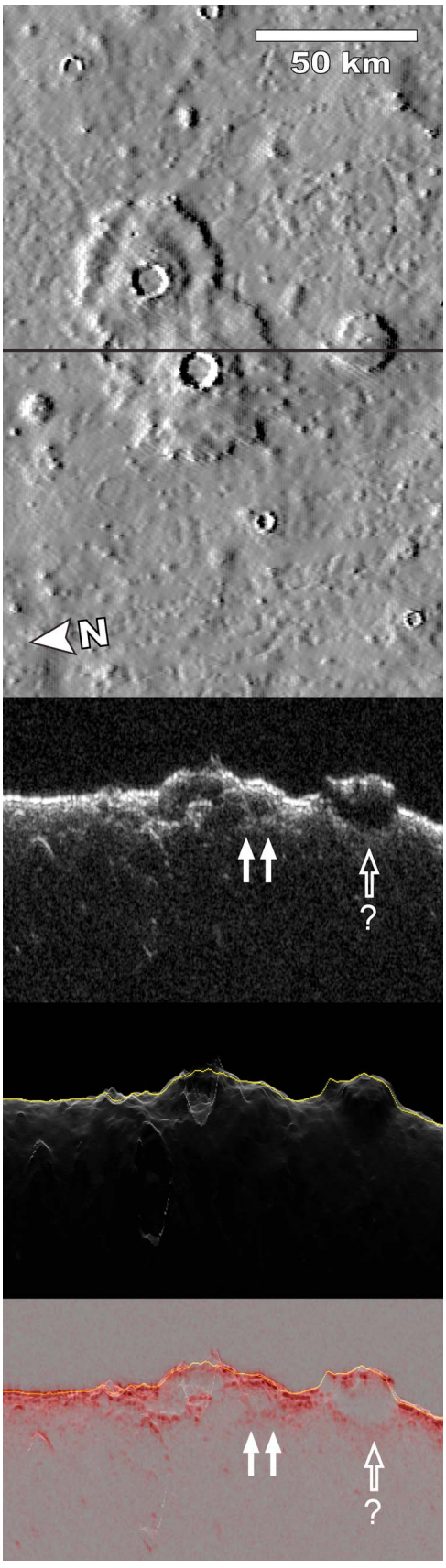

gram in Figure 6 contains the best evidence thus far for a subsurface reflection among SHARAD observations of this pedestal, which is highlighted by the arrows. To the north side of the crater a weak return at ~5.25 μs after the surface reflection is not reproduced by the cluttergram and likely represents a subsurface interface. Another weak reflection exists to the southern portion of the pedestal, starting at approximately the same delay as the northern reflection but meeting with the surface reflection at the same location where the pedestal grades into the surrounding terrain. Although this southern feature does not have a counterpart in the cluttergram and appears to be a real subsurface feature for this radargram, SHARAD product ID 797201, it appears collocated with clutter features in other tracks. To complicate matters further, these two radar features do not appear in all of the 19 radargrams covering this pedestal. We tentatively conclude that the northern reflection indeed corresponds to the subsurface interface between the pedestal and the underlying Noachian to Early Hesperian substrate [e.g., *Leonard and Tanaka*, 2001; *Tanaka and Scott*, 1987; *Williams et al.*, 2009], but are less certain for the southern reflection. No signs of internal layering are seen in the SHARAD data set for this pedestal.

[19] In the Parva Planum area of the Dorsa Argentea Formation is the location of what has been previously recognized as a large pedestal crater [e.g., *Head and Pratt*, 2001; *Tanaka and Kolb*, 2001], located at 76.06°S, 248.35°E and dubbed LPP here. This pedestal is very symmetrical, has a median width of 36 km, its perimeter lacks sinuosity and is defined by a steep scarp, and its surface stands ~500 m above the surrounding terrain. Unlike the cases examined so far, LPP is only a factor of 2.1 wider than its central crater (i.e., P/C = 2.1). Its radar signature is characterized by echoes following the surface reflection for all of the 25 radargrams examined, but a comparison to clutter simulations, as shown in Figure 7 for SHARAD product 905901, shows that those echoes are produced by surface relief likely to be the marginal scarp of the pedestal. There is no evidence for a basal reflection or internal layering from SHARAD at LPP.

[20] The pedestal population of the northern midlatitudes is the most numerous [*Barlow*, 2006; *Kadish et al.*, 2009], but this abundance includes few large, prominent pedestals, such as seen in the south. Figure 8 shows a pedestal doublet in Acidalia Planitia (51.08°N, 347.51°E, dubbed AcPD here), with the pedestals spanning 50 km and 42 km. The central craters have diameters of 11 km and 9 km, respectively, which in turn yields pedestal-to-crater ratios of 4.6 and 4.4, respectively. The margins of AcPD are well defined, symmetric, and of low sinuosity, except for the area between the two craters where the overlap relationship between the two pedestals, if any, is hard to distinguish. MOLA profiles from individual shots reveal a height of approximately 100 m

Figure 8. SHARAD radargram 16255 of a large pedestal doublet (51.08°N, 347.51°E) in Acidalia Planitia with the accompanying MOLA DEM, ground track, and clutter simulation. White arrows denote features in the radargram that do not have equivalents in the cluttergram and, therefore, likely correspond to subsurface reflections. Ghost arrows denote features in the radargram that are difficult to discern as either clutter or subsurface.

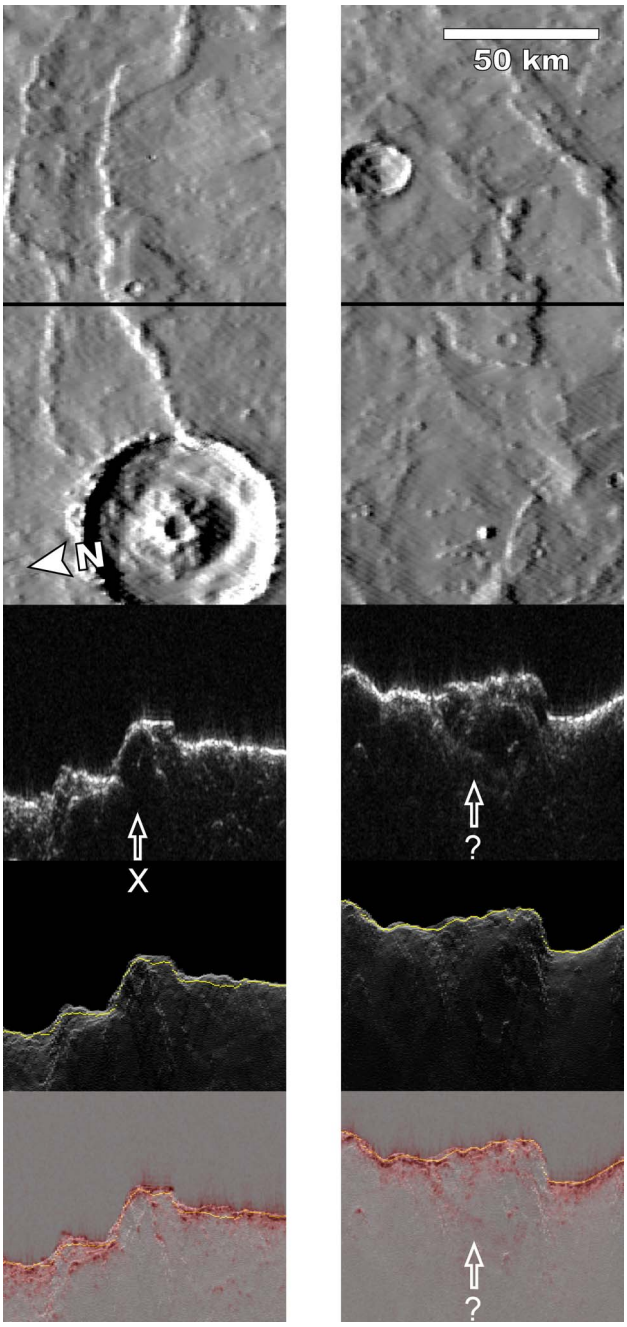

Figure 9. SHARAD radargram 743201 sampling two small pedestal craters (66.07°S, 43.39°E) in Malea Planum with the accompanying MOLA DEM, ground track, and clutter simulation. Outlined arrows denote features in the radargram that either are difficult to discern as either clutter or subsurface (question mark) or the absence of echoes following the pedestal surface reflection (cross).

above the surrounding terrain for AcPD, and that the eastern pedestal (upper in the DEM panel of Figure 8) is transitional to rampart ejecta morphology. SHARAD coverage of these pedestals is relatively sparse, with five out of eight transecting the western pedestal (lower), and most have a signature similar to that shown in Figure 8. Where the ground track crosses the western pedestal to the south of its crater, an echo unmatched by clutter simulation arrives between 1.88 μs to 2.25 μs after and 7 dB to 10 dB weaker than the surface reflection. We interpret this late echo as a result of a dielectric contrast between the pedestal and underlying surface. The shorter delay between the surface and the subsurface reflections, in comparison to the large southern pedestals (>130 m high) is consistent with the small height (80 m) of the pedestal doublet in Figure 8. To the north side of the crater, the radar signature is more variable in all of the radargrams and often matched by features in the respective cluttergrams (as in Figure 8). No radargrams at this location show evidence for internal layering.

2.3. Smaller Pedestals

[21] Immediately to the south of the large pedestal doublet in Figure 8 lies a smaller, 17 km wide pedestal, dubbed here AcSP, which stands ~130 m above the surrounding terrain. The central crater has a diameter of 3.5 km, giving it a pedestal-to-crater ratio of 4.86, similar to the neighboring doublet. At the time of this writing there is only one radargram that transects this small pedestal near its central portions. The radargram clearly shows a well-defined echo following the surface reflection from the pedestal. In time domain, which is the case in Figure 8, this echo is u-shaped and meets the surface reflection at the edges of the pedestal. The two sloping sides of this "u" closely match features in the clutter simulation and correspond to surface reflections from the edge of the pedestal. The central portion of this "u," however, does not seem to have an equivalent feature in the cluttergram, is marked by the outline of an arrow in Figure 8, and follows the surface reflection by approximately 2.3 μs. We tentatively interpret the radar signature at this pedestal as a combination of clutter and subsurface echoes.

[22] We examined nearly seventy pedestals in the northern lowlands having dimensions similar to the small pedestal in Figure 8 or smaller. For each location known to have a high concentration of pedestals, as illustrated by the map of *Kadish et al.* [2008, Figure 1] (e.g., Acidalia, Arcadia, and Utopia Planitiae) we randomly selected pedestal craters; some already had incidental SHARAD coverage while other had to be individually targeted. We find that in all that appear to have a subsurface component to their radar response, it is difficult to determine whether the echoes following the surface reflection are due to clutter or subsurface reflectors. Given their small diameters, it is rare to have more than a couple of radargrams crossing their domains in a centered fashion, which would place pedestal margins the farthest from the ground track, so it is challenging to resolve this ambiguity. Such difficulty is not exclusive to northern pedestals, either. Figure 9 contains examples of small pedestals in Malea Planum to the east of Pityusa Patera. A small pedestal doublet is seen on Figure 9 (right) and dubbed SMD here. The western (right) pedestal is clearly more extensive (~27 km along the north-south direction and ~17 km east-west), and is clearly overlain by the eastern pedestal (~18 km across). Their respective crater diameters are 5.9 km and 5 km, with 3.7 and 3.6 for pedestal-to-crater ratios. Topographic profiles constructed from individual MOLA shots reveal the southern margin as being taller (~250 m) than the northern margin (~130 m), which could be due to differential erosion, to the pedestal complex being at the edge of a local depression, or to the combination of both effects. The two radargrams crossing

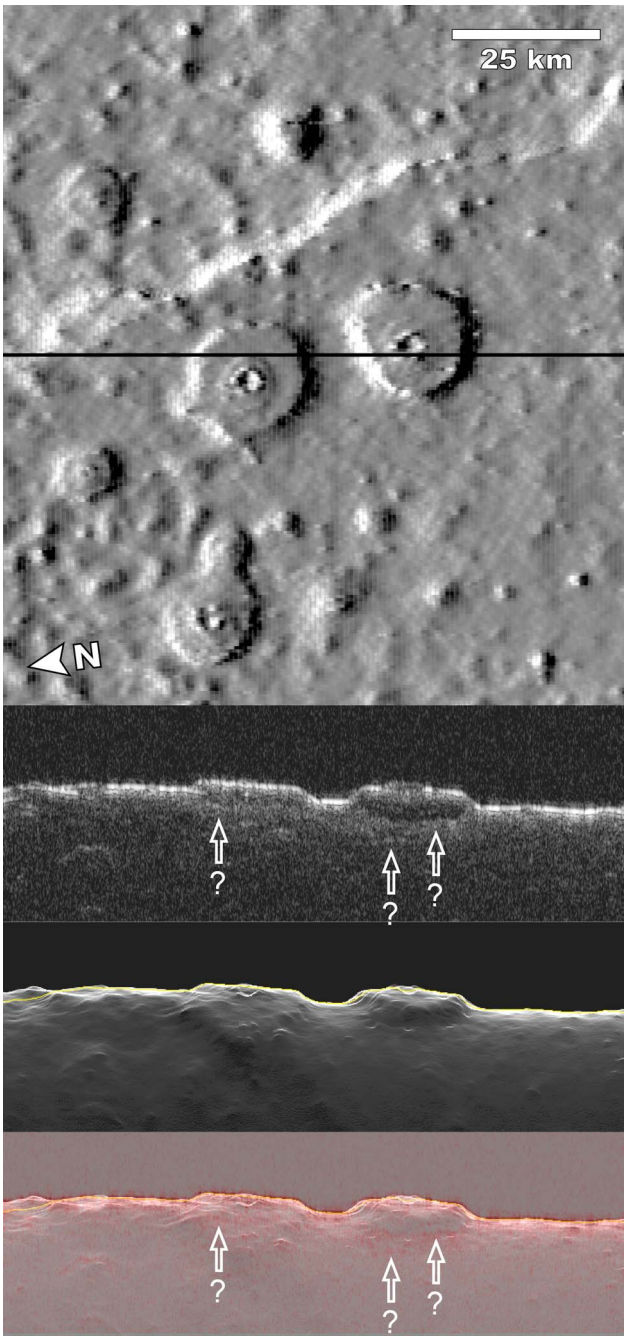

Figure 10. SHARAD radargram 13139 sampling two small pedestal craters (62.61°N, 99.42°E) in Utopia Planitia with the accompanying MOLA DEM, ground track, and clutter simulation. Ghost arrows denote features in the radargram that either are difficult to discern as either clutter or subsurface (question mark).

this pedestal doublet near its central portions show similar radar response, with 743201 depicted in Figure 9. Again, a well-defined echo having an upward concave shape appears to follow the reflection produced by the surface of the pedestal. The sides of this late reflection match predicted clutter, but not its central portions. As in the case of the small pedestal in Figure 8, this case is challenging to interpret; we again tentatively attribute the late echo to a combination of clutter and a subsurface reflection deriving from the contact between the pedestal and the underlying material. This same SHARAD radargram crosses another small pedestal to the north of and similar lateral dimensions as the small doublet. Curiously, it lacks any indication of subsurface echoes.

[23] A final example, seen in Figure 10, focuses on the two small pedestals in Utopia Planitia (62.61°N, 99.42°E, here dubbed USD) studied by *Kadish et al.* [2008], who interpreted the marginal pits surrounding the pedestals as evidence for sublimation and the ice-rich nature of the material composing USD. The northern and southern pedestals are nearly circular, span 20 km and 17 km, and have pedestal-to-crater ratios of 5.7 and 4.6, respectively. Their surfaces stand ~100 m above the surrounding terrain, as measured in MOLA shot profiles and shown in Figure 3. There are five SHARAD radargrams for each of these pedestals and they bear similar signatures; Figure 10 shows radargram 1625101 as an example. In the case of both pedestals, echoes following the surface reflection appear to show a subsurface reflector, but, again, most are matched by equivalent features in the cluttergram and do not correspond to subsurface features. In the case of the southern pedestal, however, a late reflection does not appear to have a clutter origin and is marked by the lowest contoured arrow and a question mark. This possible subsurface reflection is weak and only appears beneath a small portion of the pedestal. So, again, interpretation of the radar signatures at small pedestals is difficult and ambiguous.

3. Dielectric Modeling

[24] In most of the cases of large pedestals we examined, SHARAD radargrams reveal subsurface reflections that we have interpreted as the interface between the deposits composing the pedestals and the underlying surface. The delay of a basal reflection with respect to the surface reflection depends on the thickness and the bulk permittivity of the pedestal deposit. The thickness, however, can be estimated by simply assuming it to be equal to the height of the pedestal above the surrounding terrain measured from the MOLA shot data set. Permittivity of the pedestal material is unknown; determining its magnitude would serve as a compositional constraint to the pedestal and is the goal of this section. To do so, we convert each radargram of interest from time domain, as in Figures 1–10, to depth corrected. This is accomplished by multiplying a factor of $1/\sqrt{\varepsilon}$ to the vertical coordinate of all points following the surface reflection throughout the radargram. The factor is not applied to points preceding the surface reflection because they correspond to free space (i.e., $\varepsilon = 1$), which is adequate for the Martian atmosphere [e.g., *Leuschen et al.*, 2003; *Mouginot et al.*, 2009]. Since $\varepsilon > 1$ for the subsurface, the portion of depth-corrected radargrams following the surface reflection appears compressed vertically in comparison with the time domain version, and the greater the value of ε applied, the greater the compression (Figure 11). Although this procedure essentially assumes that the subsurface is dielectrically homogeneous and affects both subsurface reflections and clutter, we focus only on the depth of the subsurface reflections of interest. Given our assumption that the height of the pedestal above its surrounding terrain corresponds to the thickness of the pedestal deposit, the value of ε that best suits the pedestal material is that which causes the basal reflection to line up in the vertical sense with

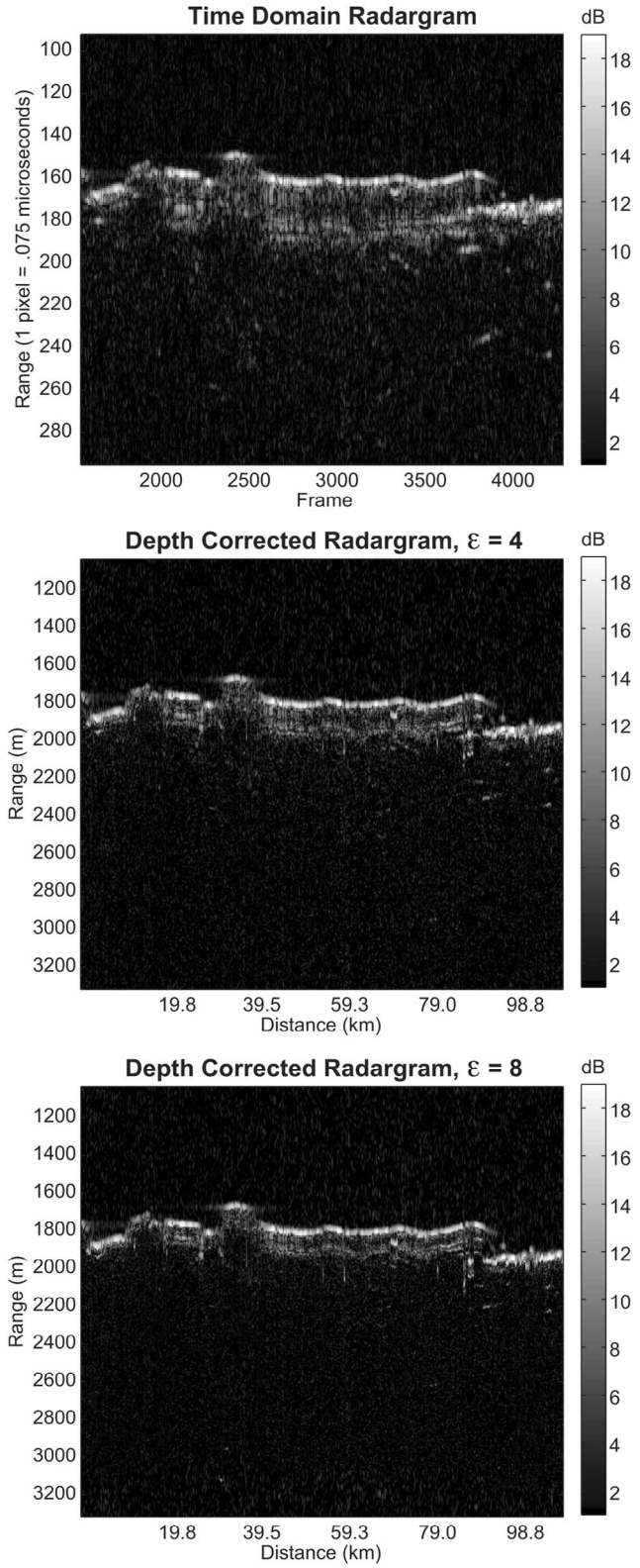

Figure 11. Time domain SHARAD radargram 748401 (top) for the largest pedestal in Malea Planum and the accompanying depth-domain versions using permittivity values of (middle) 4.5 and (bottom) 8.0. Color bar indicates the relative power in dB of the radar returns. Vertical axis corresponds to a relative measure of height in meters referenced to the top of the radargram (sample 1, clipped from figures).

the surface reflection of the surrounding terrain. Such a procedure has been used previously for other deposits on Mars, most notably the Medusae Fossae Formation [*Carter et al.*, 2009; *Watters et al.*, 2007], the polar layered deposits [*Phillips et al.*, 2008; *Picardi et al.*, 2005], and the lobate debris aprons [*Holt et al.*, 2008; *Plaut et al.*, 2009]. Figure 11 shows a section of the time domain version of SHARAD radargram 748401 of the largest pedestal in Malea Planum (Figure 2a) along with depth-domain radargrams for ε = 4.5 and ε = 8.0. The higher permittivity clearly produces excessive vertical compression, causing the basal reflection beneath the pedestal to stand higher than the surrounding terrain, while the lower of the two values produces the best alignment. We find that there is a variation of ±0.5 in permittivity for the best alignment in all of the radargrams available for this pedestal, so we conclude that the bulk permittivity for this pedestal is 4.5 ± 0.5. Similarly, we obtained a permittivity value of 3.8 ± 0.3 for LMP3 in Figure 6. In the case of LMP2, Figure 5, a contrast exists between the north and south sides of the pedestal, where the former consistently yields a permittivity value of ~3 and the latter ~4. In an attempt to be more precise with extracting the permittivity, we examined individual records (vertical lines) in the radargrams to pick more precisely the arrival time of the surface and subsurface echoes before applying the time-to-depth conversion. Figure 12 shows the results of this exercise for individual tracks, where the vertical offset between a subsurface reflector and the surrounding terrain is given as a function of permittivity. An offset of zero at a given ε value therefore fulfills the assumption that the base of the pedestal

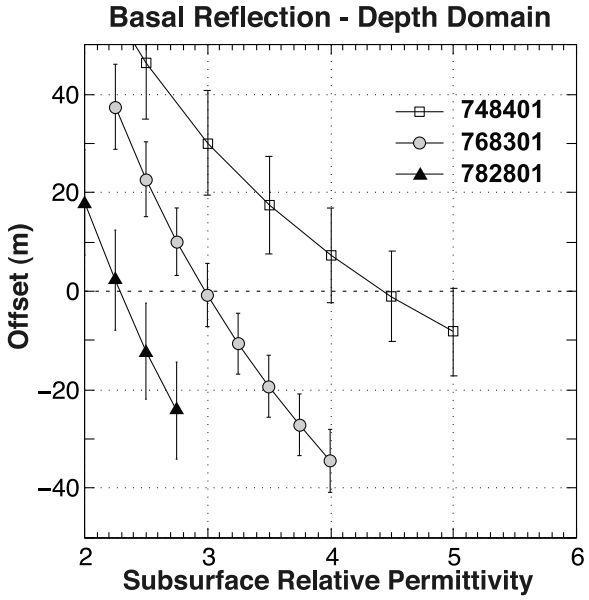

Figure 12. Vertical offset between the basal reflector and the surface adjacent to the pedestal obtained in depth domain for various permittivity values. Error bars correspond to one standard deviation across all of the frames examined along the basal reflector. SHARAD tracks 782801 and 768301 are for the pedestal in Figure 5, while 7484 is for the pedestal in Figure 4. An offset of zero yields an estimate of permittivity, assuming the reflector is at the same elevation as the surroundings.

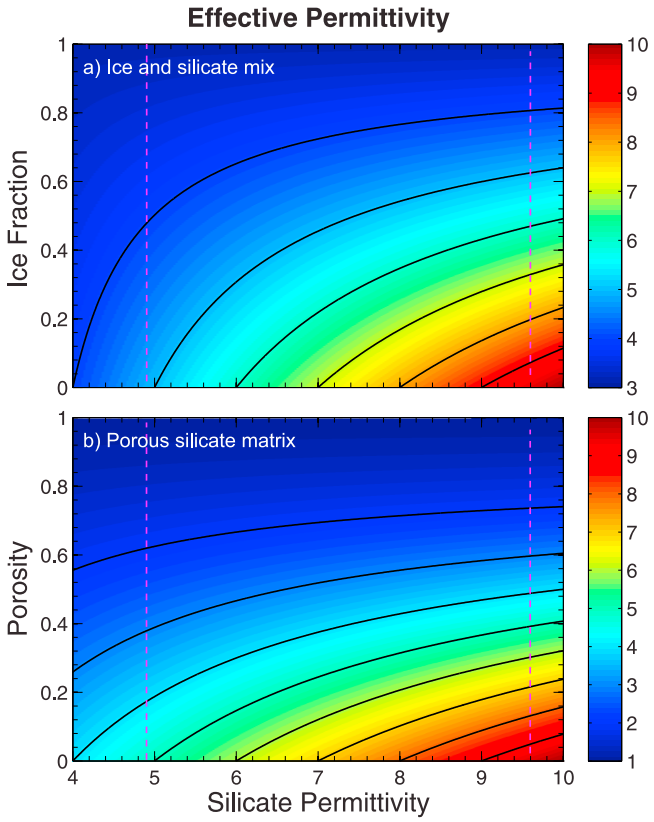

Figure 13. (a) Color map showing the effective permittivity ε'_{mix} of a mixture of water ice and silicates of various proportions obtained with the deLoor mixing model, with ε'_{ice} = 3.15. Heavy black curves denote contours of constant effective permittivity. Vertical dashed lines correspond to the bounds of the permittivity envelope for silicates according to *Ulaby et al.* [1986]. Inclusion fraction values of 0.0 and 1.0 correspond to pure silicate and pure ice, respectively. (b) Same as Figure 13a except for a silicate matrix of varying porosity values.

deposit and the surrounding surface correspond to the same interface. In the case of LMP2 (Figure 5), the difference in permittivity from one side of the pedestal to the other still remains: $\varepsilon = 2.3$ for the northern side (radargram 782801) and $\varepsilon = 3.0$ for the southern side (radargram 768301). Despite the difference, the permittivity values are overall lower than what was obtained previously. The error bars come from averaging the offset along a reflector segment from which the samples were extracted. The third curve in Figure 9, for SHARAD track 748401, corresponds to LMP1 (Figure 2a) and yields a pedestal permittivity of 4.4, which is consistent with what was estimated in section 2. Not included is the permittivity for AcPD (Figure 8), which yielded $\varepsilon_{mix} = 4.0$, which translates into either an ice/silicate mixture or a porous silicate.

[25] The small pedestal SMD (Figure 9) was found to have $\varepsilon = 6 \pm 0.5$. A value of $\varepsilon = 4.9$ is at the lowest threshold for the most common mafic and altered rocks and higher than that of water ice, as described in Table 1. Consequently, it is reasonable to expect that either a mixture of ice or empty pore space and high-permittivity (>6) silicates or a low-permittivity (~6) silicate matrix makes up most of the small pedestal deposits we observed. Not enough information is available in the SHARAD data alone to eliminate this ambiguity.

[26] To turn the bulk permittivity estimates into compositional constraints, it is necessary to assume permittivity values for the main components of the material composing the pedestal deposits and to apply them to mixing formulas according to various proportions. There are different mixing models that make different assumptions about a given mixture of materials, such as the shape and distribution of the inclusions in a given material host [e.g., *Ulaby et al.*, 1986]. *Nunes and Phillips* [2006], for example, adopted two mixing models in calculating the effective permittivity of ice with variable amounts of silicate inclusions to construct a dielectric model of the Martian polar layered deposits. Both of these models, deLoor and Tinga-Voss-Blossey, assume randomly distributed spherical inclusions much smaller than the wavelength of the radar wave [*Ulaby et al.*, 1986], but the two formulations differ from each other in how they consider the effects of the host material immediately surrounding the inclusions. Figure 13a shows the effective permittivity of the mixture, ε_{mix}, using the deLoor mixing formula with ε'_{ice} = 3.15 and $4.0 \leq \varepsilon_{sil} \leq 10.0$ for different inclusion fractions. At inclusion fractions of 0.0 and 1.0 the material corresponds to pure silicate and pure ice, respectively. The greater the permittivity assumed for the silicate, the greater the ice fraction needs to be in order to maintain a given ε_{mix} value. The area in this plot that corresponds to the large pedestals in Malea Planum is that between the $\varepsilon_{mix} = 4.0$ and $\varepsilon_{mix} = 5.0$ contours. For the lowest plausible silicate permittivity value of 4.9 [*Ulaby et al.*, 1986], the fraction of ice needs to be between 0.00 to 0.48 to satisfy the range in ε_{sil}. Similarly for the highest silicate permittivity value of 9.6 [*Ulaby et al.*, 1986], the fraction of ice needs to be between 0.63 and 0.81. In either case, a fraction of ice ≥20% is implied for the LMP1 (Figure 4) pedestal material, for which we measured ε_{mix} = 4.5. In the case of LMP2 (Figure 5), the range in permittivity values obtained ($2.3 < \varepsilon_{mix} < 3.0$) is lower than that of pure, bulk water ice and cannot be explained by the mixing of silicates and ice alone – we discuss the implication of this case in section 4. Note that if employing the Tinga-Voss-Blossey mixing formula, then the slope of the contours in Figure 13 becomes flatter, thus reducing the ice content estimates by no more than ~10%.

[27] As previously mentioned, it is also plausible that the material in the pedestals consists of porous silicates. Figure 13b shows the effective permittivity values for a porous silicate matrix obtained with the deLoor mixing formula with ε_0, $4.9 \leq \varepsilon_{sil} \leq 9.6$, and different porosity values. Obviously, zero and unity porosities correspond to a solid silicate and free space, respectively. The greater the permittivity assumed for the silicate, the greater the porosity needs to be in order to maintain a given ε_{mix} value. Because free space has a lower permittivity than water ice, less porosity is needed than ice fraction in order to produce a given value of ε_{mix}, which can easily be confirmed by comparing Figures 13a and 13b. For the lowest silicate permittivity value of 4.9 [*Ulaby et al.*, 1986], the porosity needs to be between 0.2 and 0.4 for the pedestals with permittivity between 3 and 4 (e.g., Figure 5), and between 0.0 and 0.2 for the pedestals with permittivity between 4 and 5 (e.g., Figure 4). For the highest silicate permittivity value of 9.6 [*Ulaby et al.*, 1986], in turn,

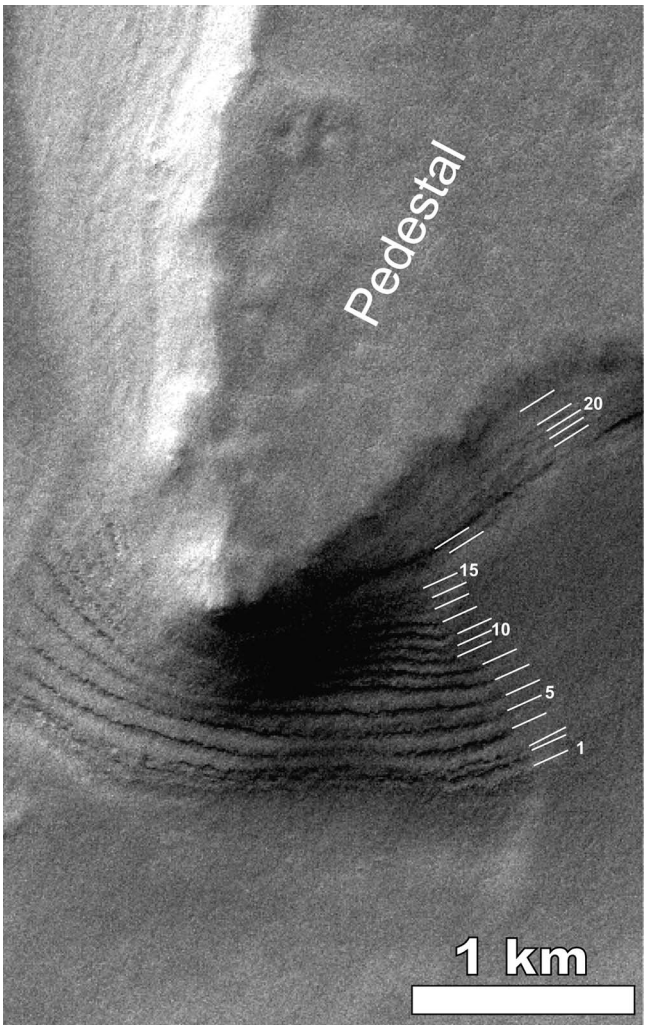

Figure 14. Portion of MOC frame S16/01895 showing fine layering at the marginal scarp of the large Malea pedestal from Figure 2a. We count 22 layers, as marked, though layers above 13 are harder to see in this stretch. A mantle layer is present at the base of the scarp and in some places blankets the marginal layers all the way to the top of the pedestal.

the porosity needed lies between 0.5 and 0.6 for the pedestals with lower permittivity, or between 0.4 and 0.5 for pedestals with higher permittivity.

[28] Of the small pedestals examined, we only estimated the permittivity for the doublet in Malea Planum (Figure 9), which turns out to be 6.0. Adopting $6.0 \leq \varepsilon_{sil} \leq 9.6$, the ice fraction needs to be within 0.0 and 0.5, or the silicate porosity between 0.0 and 0.3 in order to keep the effective permittivity compatible with that of the small pedestal.

4. Discussion

[29] As seen in sections 1–3, pedestals present a variety of radar signatures, and perhaps the most curious aspect is the differences among the different large pedestals. The possible range in ice-to-silicate ratio also spreads quite widely, from 0.0 to 0.8, throughout the parameter space. Given this degree of uncertainty, we investigate data sets other than SHARAD to understand the possible source for those differences.

[30] The largest of the pedestals, LMP1 (Figure 2a), possesses a dielectric permittivity of ~4.5, consistent with either a porous silicate or an ice-silicate mixture, and multiple internal reflections strongly indicative of layering in the deposit. We have conducted a survey of both MOC and HRSC imagery and determined that layering is also visible on the marginal scarps of this pedestal. Exposures are not continuous, tend to occur in short segments, and are concentrated on the southern margin between azimuths 100° and 280°. Figure 14 shows an example of an exposure where layering is seen at the extremity of one of the pedestal "toes." Here we count 22 layers, which appear to be laterally continuous for several kilometers along the sinuous perimeter and evenly spaced in the vertical sense. Assuming an uncertainty of 100 m in the determining the elevation of a given layer, which is reasonable given the thickness of the pedestal deposit is ~150 m, a back-of-the-envelope calculation yields a layer slope of atan(100 m/5 km) = 1°; this suggests the layers are largely horizontal. Layers appear to be exposed in a stair-step fashion and are more easily distinguished where the exposure has a shallower slope. To assist in the counting the number of layers, we gradually changed the stretch of the gray scale in order to highlight the upper layers. Figure 15 shows that the individual MOLA shots are too coarsely separated to resolve relief at the scale of the layers. Given that the height of the pedestal is on the order of 140 to 160 m, we calculate an average layer thickness between 6.3 and 7.3 m. The fact that we can only count ~10 layers in the radargrams suggests that SHARAD reflections from two consecutive individual layers are interacting to produce a single echo. This type of effect was predicted for the fine layering of the Martian NPLD by *Nunes and Phillips* [2006]. So, if the average layer thickness from MOC/MOLA is assumed to be the vertical resolution limit of SHARAD for the pedestal material, the bulk permittivity is then (resolution in free – space/resolution in material)^2, or $4.2 \leq \varepsilon' \leq 5.6$; this also serves as a rough estimate on the bulk permittivity of this deposit. Given the difficulty of counting the number of layers in the upper portion of the pedestal in Figure 14, consider that the 15 clearly visible layers in Figure 15 correspond to a thickness of 80 m, which yields a mean layer thickness of 6.2 m – essentially the same as before.

[31] Interspersed with the exposures of layering along the margin are longer segments where a mantling layer, present throughout the surrounding terrain, overlaps the marginal scarp all the way to the crest of the pedestal. Where the mantle is thicker, the pedestal layering is completely obscured. Where the mantle is thinner, a subtle expression of relief from the underlying marginal layers can be seen. This mantle is very smooth at the scale of MOC, CTX, and HRSC, similar to the undissected surface mantle of *Mustard et al.* [2001] that was interpreted to bear pore ice. Examination of two HiRISE images of the margin of LMP1 (ESP_014031_1125 and ESP_014308_1135) shows the presence of very fine polygonal cracking of the mantle covering the terrain surrounding the pedestal, the pedestal marginal slopes, and the pedestal surface. Polygonal cracking is thought to signal present or past ground ice in the regolith [e.g., *Levy et al.*, 2010] and is seen at other sites where shallow subsurface ice has been detected (Phoenix landing site [*Mellon et al.*, 2009] and site of fresh small impact craters [*Byrne et al.*, 2009]). However, this mantle does not appear to produce a reflection in the

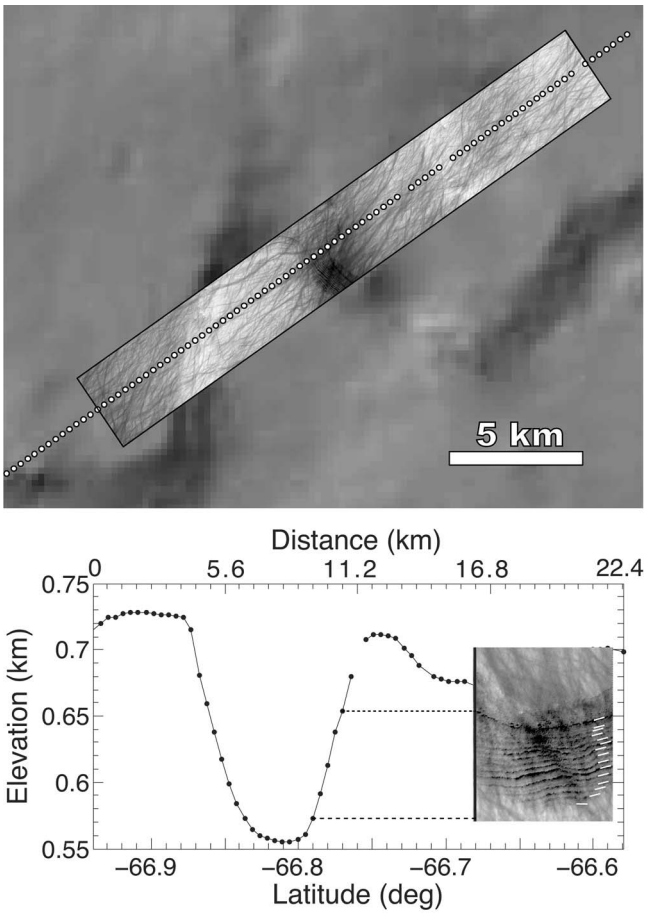

Figure 15. (top) Individual MOLA shots from PEDR ap12655 across the margin of the Malea Pedestal in Figure 2a, superposed on MOC frame R11/04399 and shaded relief depiction of the 128 pixel/degree MOLA gridded data. (bottom) Topographic profile from the MOLA ap12655 shots and the MOC. Height of the pedestal is about 150 m, and fine layering is exposed on both of the scarps sampled by the profile (at ~4 and 11 km). MOLA shot separation is too coarse to resolve the layers.

SHARAD radargrams at this location either because it is too thin to be resolved or it does not present a large enough contrast in permittivity to produce a reflection. Note also that the radar reflection from the surface of the pedestal is nearly specular, which indicates a dearth of surface scattering, implying a smooth surface at SHARAD wavelengths (15 m). This observation stands in great contrast with those of *Nunes et al.* [2010], which show the surface reflection from non-pedestal ejecta blankets to be very diffuse as a result of surface scattering. Hence, ejecta blankets are rougher than the surface of pedestals from MOLA scales (~400 m) down to SHARAD wavelengths (15 m).

[32] Based on the image data we believe that the mantle unit has been or currently is being removed to expose the layered material composing the pedestal. There is no evidence for overhangs and debris slumping, as might be expected from preferential removal of the pedestal material beneath an armoring surface. Based on the possibility that the mantle is being actively removed, or at least that the pedestal layering exposures are recent, we searched the data set from the CRISM (Compact Reconnaissance Instrument Imaging Spectrometer) [*Murchie et al.*, 2007] for another constraint to the compositional nature of the largest Pedestal in Malea Planum. Only one CRISM footprint is close enough to a relatively minor exposure, as seen in Figure 16, where a few pedestal layers are partly revealed. These layers are shown in the IR band as well as in the mafic band 1 (MAF1), but they are absent from the ices band (ICE1). *Pelkey et al.* [2007] offer a detailed description of these bands prepared by the CRISM team as browse summary products. In MAF1, the green and blue hues are indicative of low-Ca and high-Ca pyroxenes. Close investigation of the actual spectra corrected for the atmosphere reveals a gentle positive slope around 1 μm, which is indicative of mafic, iron-bearing mineralogy. Because the 1 μm slope is gentle, the layering visible in the frame is barely exposed through a mantle unit, and because this exposure is not well centered in the CRISM frame, we interpret the mafic composition as only tentative at this point. We note that low albedo material collecting in two neighboring volcanic calderas appear to have a basaltic composition according to HRSC (High Resolution Stereo Camera) [*Jaumann et al.*, 2007] and OMEGA (Observatoire pour la Minéralogie, l'Eau, les Glaces et l'Activité [*Bibring et al.*, 2004], so mobile mafic fines are regionally available. More targets were placed at the margins of the large Malea pedestals at the time of this writing, and we await better data to confirm this finding. Nonetheless, the fact we see a possible mafic signature associated with the layers supports the finding from the dielectric modeling of SHARAD data (ε = 4 to 5) that the material in pedestal deposits contain a significant fraction of silicates (Figure 13). Further, the absence of ice signatures in CRISM data does not invalidate the possibility raised by the dielectric models that a substantial fraction of ice may also exist in pedestal materials (Figure 13) because, if exposed, ice is unstable at Martian surface conditions and will rapidly sublimate.

[33] Both of the other large pedestals in Malea Planum have a mantling layer similar to the ones described, but their margins lack clear exposures of the underlying pedestal material. In the case of LMP3 (Figure 6), hints of layering are seen where the mantle overlapping the pedestal margins is apparently thin, similarly to what is seen on the left side of the LMP1 pedestal lobe in Figure 14. Oddly, none of the available SHARAD radargrams of this pedestal show any layering. A number of possible effects may explain this absence. Slope in the pedestal layers would reduce the power reflected back to the SHARAD antenna, and so would weaker dielectric contrasts across the layers. Another possibility is that the dielectric properties of the mantle at this location are different from the other layered pedestal and reduces the coupling of the signal into the subsurface. A combination of these or other factors could also be claimed, but a systematic study of each factor is necessary to better understand the problem. The point that should be kept in mind is that the internal reflections produced by layering within LMP1 are weak and can be more easily depressed below the noise level than the basal reflection at other pedestals (such as LMP3).

[34] The low permittivity value (2.3) for the northern section of LMP2 (Figure 5) is difficult to interpret. One possibility is that this portion of the deposit is dominated by porous ice, but this does not seem to be very likely because porosity

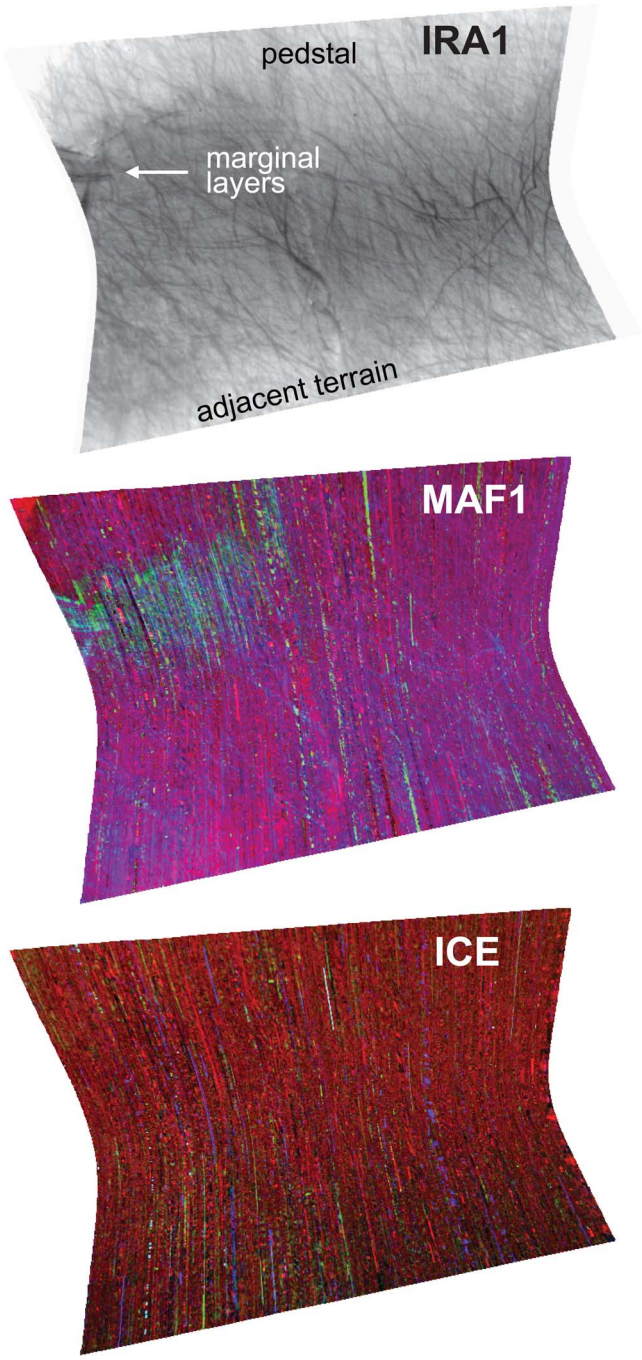

Figure 16. CRISM product FRT0001461F_07_IF163S, centered approximately at 66.4°S and 60.3°E, showing a section of the margin of the large Malea pedestal in Figure 4. A minor partial exposure of pedestal layers is seen in the upper left of the frame. From the top to bottom, derived spectral products correspond to IR surface brightness (IRA1), mafic mineralogy (MAF1), and water and CO_2 ice (ICE1A). A trace of mafic mineralogy is seen at the layering, while no ice signature is observed.

in ice tends to decrease over time due to compaction under the weight of the overburden [e.g., *Arthern et al.*, 2000] and a porous matrix would likely be more susceptible to deflation (for example, see the summary of *Augustinus* [1991]). Another alternative is that this portion of the pedestal is dominated by a very porous silicate matrix, but this probably suffers from increased susceptibility to deflation. More likely perhaps is the breakdown of our assumption that the subsurface reflector corresponds to the interface between the pedestal material and the surrounding surface. It is possible that the subsurface reflector seen on the left side of the radargram in Figure 5 is due to an interface other than the surrounding surface. If the subsurface reflection in question were to be produced in an interface higher than the base of the pedestal (as in one of the internal layers), then it would require a lower value of ε to bring it to the same level as the surrounding terrain in a depth-corrected radargram (such as what is observed). It is not clear, however, why an internal layer would produce a strong reflection at this location only. In contrast, a pedestal basal interface deeper than the surrounding terrain would necessitate a higher value of ε, which is not the case. Finally, there is the possibility of basal relief that pushes the interface to a level higher than the surroundings, which may be the more likely scenario.

[35] The large pedestal in Parva Planum (LPP) is notably different from the large pedestals in Malea, not only in the absence of a subsurface radar signature, but also in its morphology. Its marginal scarps are very steep and mostly covered with what appears to be a fine-grained debris blanket different from the mantling described in the previous cases. There are no indications of layering at the margins. The only layering observed is on the western surface of the pedestal and deep within the bowl of the central crater. This layering appears to be associated with the material blanketing the surface of the pedestal, which is very smooth and gently undulating, and shows fine fracturing at HiRISE scales. Reasons why a basal reflection is not present in this case can range from a lack of substantial dielectric contrast between the pedestal and the underlying surface, to the pedestal material being much lossier due to higher electric conductivity (as in the case of mafic composition indicated by CRISM at one of the Malea pedestals) or to volume scattering. Given that the pedestal is the thickest of all of the ones examined (>500 m), path losses are likely to be greater here even if the material composing the pedestal were similar to the large pedestals of Malea Planum. However, the Dorsa Argentea Formation, which stratigraphically underlies LPP, is thought to be ice-rich [e.g., *Head and Pratt*, 2001]. If so, the dielectric contrast could perhaps be negligible with respect to ice-rich pedestal deposits. A combination of these two factors may explain the lack of observed subsurface reflections at LPP.

[36] The large pedestal doublet in Acidalia Planitia is very sparsely imaged at high resolution, and we were not able to examine its entire perimeter. Based on a single CTX frame, there are no indications of layering exposed at the margins. A few pits, similar to those identified at small pedestals by *Kadish et al.* [2008], are present along small segments of the perimeter, as well as isolated blocks apparently derived from the pedestal due to the loss of material along polygonal cracks. The smaller pedestal to the south of the doublet possesses a comparable morphology.

[37] The small pedestal doublet in Malea Planum, just to the east of Pityusa Patera, seen in Figure 9, appears to in a local depression. To the south and the southeast, the margin of the pedestals are elevated with respect to lowest point in

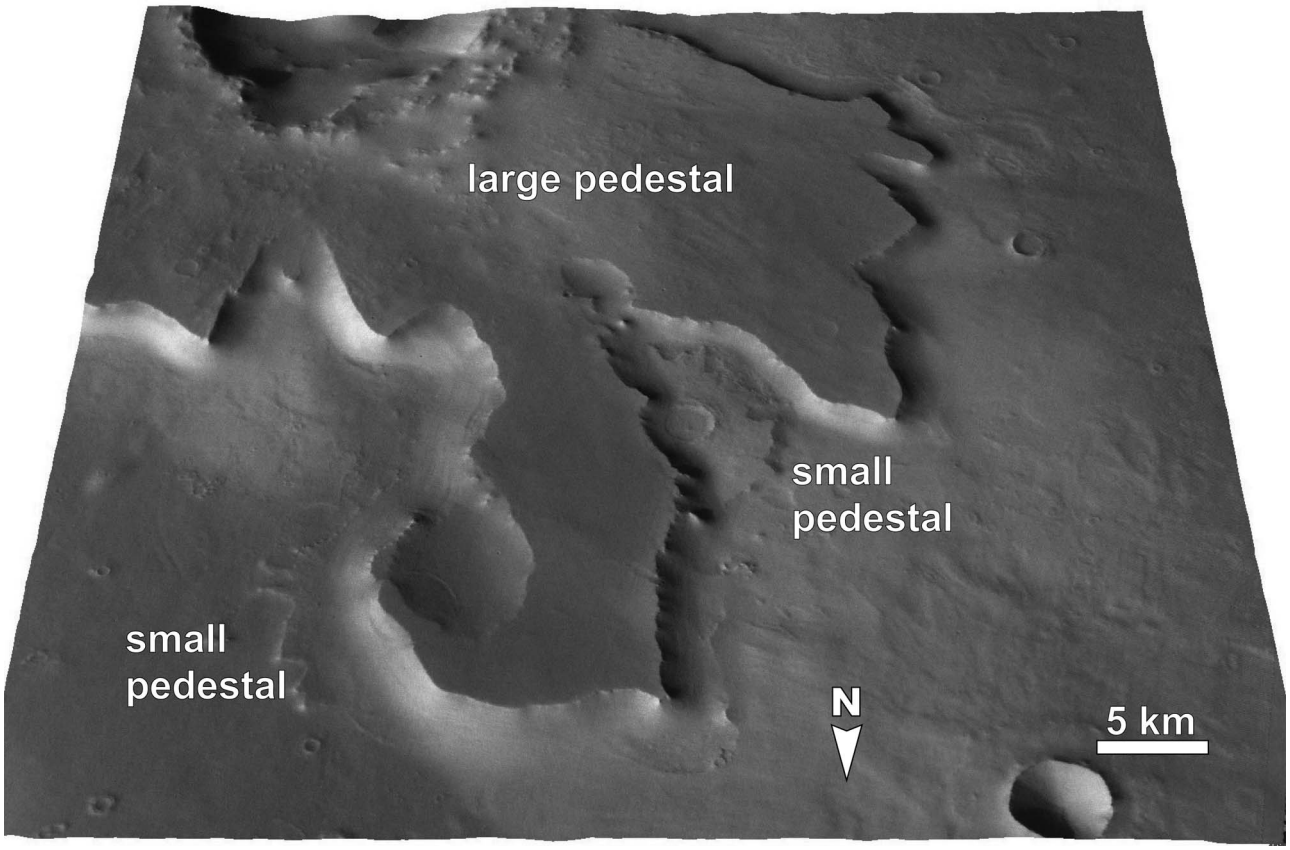

Figure 17. Perspective view of HRSC DEM showing the superposition of a distal lobe of the large Malea pedestal of Figure 6 (LMP3) and two other smaller (~10 km) pedestals. Image centered approximately at 71.4°S, 54.3°E. Illumination is from the lower left.

this depression. To the north, the margin of pedestal doublet merges with the margin of the rim of the depression. The area is partly mantled, but the mantle appears dissected to a greater degree than at the locations of the larger Malea pedestals. Based on MOC and HRSC images, the south and east margins of the pedestal doublet are partly devoid of mantle and present some indication of layering, but pitting is the dominant morphology. Given that the eastern pedestal overlays the western pedestal, we believe that the pedestals belong to a layered sequence, perhaps with fewer layers in the case of the larger Malea pedestal. In fact, the large Malea pedestal of Figure 6 is part of such sequence. Figure 17 shows a perspective view based on HRSC data of one of the distal lobes of this large pedestal overlying a much smaller pedestal, the latter perhaps being composed of the same layers extending from the lower portion of the larger pedestal and, thus, of the same material and of the same layers extending from the lower portion the larger pedestal. Similar stratigraphic superposition was previously noticed by *Kadish et al.* [2008] for smaller pedestals in Utopia Planitia, attributing the overlapping layers as being possibly due to cratering events during different periods of midlatitude glaciation produced by orbital forcing [e.g., *Head et al.*, 2006; *Laskar et al.*, 2002]. Here we note that this is also a plausible scenario for the larger pedestals.

[38] All of the positive identification of subsurface reflectors occurred for pedestals with P/C values greater than the 2.0 mode of the pedestal population [*Kadish et al.*, 2009]. LPP (P/C = 2.1) in Figure 7 exemplifies the lack of reflector for small P/C values, but it is also the thickest (~500 m) pedestal and the relationship between P/C and the presence of reflectors is not clear. Based on their finding of an average P/C = 3.1 for the pedestal population that is greater than the average ejecta-to-crater diameter ratios (1.7 [*Barlow*, 2006]), *Kadish et al.* [2009] argued that the armoring mechanism had to extend farther than emplaced ejecta, perhaps involving a shock wave associated with the impact event. SHARAD resolution is either insufficient to detect or the armored layer does not present a dielectric contrast to produce a shallow reflection.

[39] A genetic relationship between large (>30 km) and smaller pedestal craters is difficult to establish with the use of SHARAD alone, however, given that we could not document the unambiguous presence of a basal reflector and for the smaller diameters. We can, however, relate these two populations based on several important physical commonalities. Both small and large pedestals exhibit a defining marginal scarp around the perimeter of a flat pedestal surface. Despite the wide range in pedestal crater diameters, as previously mentioned here and by *Kadish et al.* [2010], large pedestals are not proportionally taller than small pedestals. Further, this finding extends to excess ejecta craters [*Black and Stewart*, 2008], which range from 16 to 108 m tall, and perched craters [*Boyce et al.*, 2005], which are usually <100 m but can

reach up to 250 m tall. Because pedestal heights can be used as a proxy for the thickness of the target material from which the pedestal formed, this suggests that both large and small pedestals resulted from impacts into similar deposits [e.g., *Kadish et al.*, 2010; *McCauley*, 1976]. Also, the presence of small pedestals superposed on large pedestals (top of Figure 2a), and large pedestals partially covering or sharing its lower layers with small pedestals (Figure 17) is evidence that both pedestal sizes have been capable of forming over the same time period.

5. Conclusions

[40] Large (>30 km) pedestal craters on Mars tend to be radar transparent and are consistent with a composition bearing water ice and silicates, having derived bulk permittivities generally in the range between 3 and 5. Uncertainties in the permittivity of Martian silicates leads to a broad parameter space, raising also the possibility that pedestals consist simply of porous silicate. Limited CRISM data at marginal layering exposed in one of the large pedestals in Malea Planum show tentative evidence for a mafic composition of these layers, while a spectral signature for ice is absent. Given that ice is unstable at current Martian surface conditions, the lack of evidence for ice in CRISM cannot be used to rule out the presence of ice deeper within the pedestal deposits. In fact, many ice deposits probed by Mars radar sounders lack spectral signatures of ice. Because CRISM observations are limited to only a subset of the pedestals examined with SHARAD, these conclusions cannot be generalized to the entire pedestal population.

[41] SHARAD observations of smaller pedestal craters are more difficult to interpret because reflections produced by the margins of the pedestal (i.e., clutter) tend to overprint subsurface reflections. In the few cases where a subsurface reflection was seen beneath small pedestals, derived permittivity values are higher (~6): either this reflects a more mafic composition of these deposits, or it is a consequence of the greater difficulty in distinguishing the subsurface reflector from clutter. In at least one location in Malea Planum, a partially exposed small pedestal appears to be made of the lower layers of a larger pedestal, which implies the same composition between the two size populations.

[42] The layered nature of the pedestals and their different thicknesses, along with the possibility of an icy composition, are consistent with the hypothesis that pedestals formed upon icy layers deposited at various times during midlatitudinal glaciation. Conversely, a porous silicate composition is also compatible with the permittivities yielded by SHARAD. In this case, a mechanism is needed to explain the fine layering observed at the large pedestals in Malea Planum. Based on volcanic geological context of Malea Planum and the mafic composition suggested a CRISM observation of pedestal layers, volcanic ash deposited over multiple volcanic episodes is also consistent with our results.

[43] **Acknowledgments.** We would like to acknowledge Stefania Mattei and her team at the SHARAD Operations Center for their continued dedication to provide the best quality data set possible, grazie mille a voi. We would also like to thank Eldar Noe Dobrea for discussions regarding CRISM data. Caltech's Summer Undergraduate Research Fellowship supported B. Fisher and the initial thrust of this work. D. Nunes would like to thank the support from Caltech Postdoctoral Scholar Program and the Mars Reconnaissance Orbiter program office. The authors would like to acknowledge reviews by Nadine Barlow and James Skinner, which helped improve the quality of this manuscript. This research was carried out at the Jet Propulsion Laboratory, California Institute of Technology, under a contract with the National Aeronautics and Space Administration.

References

Allen, C. C., R. V. Morris, D. J. Lindstrom, M. M. Lindstrom, and J. P. Lockwood (1997), JSC Mars-1: Mars regolith simulant, *Lunar Planet. Sci.*, *XXVIII*, Abstract 1797.

Arthern, R. J., D. P. Winebrenner, and E. D. Waddington (2000), Densification of water ice deposits on the residual north polar cap of Mars, *Icarus*, *144*(2), 367–381, doi:10.1006/icar.1999.6308.

Arvidson, R. E., M. Coradini, A. Carusi, A. Coradini, M. Fulchignoni, C. Federico, R. Funiciello, and M. Salomone (1976), Latitudinal variation of wind erosion of crater ejecta deposits on Mars, *Icarus*, *27*(4), 503–516, doi:10.1016/0019-1035(76)90166-4.

Augustinus, P. C. (1991), Rock resistance to erosion: Some further considerations, *Earth Surf. Processes Landforms*, *16*, 563–569, doi:10.1002/esp.3290160608.

Barlow, N. G. (2006), Impact craters in the northern hemisphere of Mars: Layered ejecta and central pit characteristics, *Meteorit. Planet. Sci.*, *41*, 1425–1436, doi:10.1111/j.1945-5100.2006.tb00427.x.

Bibring, J.-P., et al. (2004), OMEGA: Observatoire pour le Minéralogie, l'Eau, les Glaces et l'Activité, *Eur. Space Agency Spec. Publ., ESA-SP1240*, 37–49.

Black, B. A., and S. T. Stewart (2008), Excess ejecta craters record episodic ice-rich layers at middle latitudes on Mars, *J. Geophys. Res.*, *113*, E02015, doi:10.1029/2007JE002888.

Bleacher, J. E., S. E. H. Sakimoto, J. B. Garvin, and M. Wong (2003), Deflation/erosion rates for the Parva Member, Dorsa Argentea Formation and implications for the south polar region of Mars, *J. Geophys. Res.*, *108*(E7), 5075, doi:10.1029/2001JE001535.

Boyce, J. M., P. Mouginis-Mark, and H. Garbeil (2005), Ancient oceans in the northern lowlands of Mars: Evidence from impact crater depth/diameter relationships, *J. Geophys. Res.*, *110*, E03008, doi:10.1029/2004JE002328.

Byrne, S., et al. (2009), Distribution of mid-latitude ground ice on Mars from new impact craters, *Science*, *325*(5948), 1674–1676, doi:10.1126/science.1175307.

Campbell, B. A. (2002), *Radar Remote Sensing of Planetary Surfaces*, Cambridge Univ. Press, Cambridge, U. K.

Carr, M. H. (1979), Formation of Martian flood features by release of water from confined aquifers, *J. Geophys. Res.*, *84*(B6), 2995–3007, doi:10.1029/JB084iB06p02995.

Carr, M. H., and G. G. Schaber (1977), Martian permafrost features, *J. Geophys. Res.*, *82*(28), 4039–4054, doi:10.1029/JS082i028p04039.

Carr, M. H., L. S. Crumpler, J. A. Cutts, R. Greeley, J. E. Guest, and H. Masursky (1977), Martian impact craters and emplacement of ejecta by surface flow, *J. Geophys. Res.*, *82*(28), 4055–4065, doi:10.1029/JS082i028p04055.

Carter, L. M., et al. (2009), Shallow radar (SHARAD) sounding observations of the Medusae Fossae Formation, Mars, *Icarus*, *199*(2), 295–302, doi:10.1016/j.icarus.2008.10.007.

Christensen, P. R., et al. (2001), Mars Global Surveyor Thermal Emission Spectrometer experiment: Investigation description and surface science results, *J. Geophys. Res.*, *106*(E10), 23,823–23,871, doi:10.1029/2000JE001370.

Chyba, C. F., S. J. Ostro, and B. C. Edwards (1998), Radar detectability of a subsurface ocean on Europa, *Icarus*, *134*, 292–302, doi:10.1006/icar.1998.5961.

Craddock, R. A., and A. D. Howard (2002), The case for rainfall on a warm, wet early Mars, *J. Geophys. Res.*, *107*(E11), 5111, doi:10.1029/2001JE001505.

Cutts, J. A. (1973), Wind erosion in the Martian polar regions, *J. Geophys. Res.*, *78*(20), 4211–4221, doi:10.1029/JB078i020p04211.

Daniels, D. (2008), Ground penetrating radar, in *Radar Handbook*, edited by M. Skolnik, pp. 21-21–21-41, McGraw Hill, New York.

Edgett, K. S., B. J. Butler, J. R. Zimbelman, and V. E. Hamilton (1997), Geologic context of the Mars radar "Stealth" region in southwestern Tharsis, *J. Geophys. Res.*, *102*, 21,545–21,567, doi:10.1029/97JE01685.

Fassett, C. I., and J. W. Head (2008), The timing of Martian valley network activity: Constraints from buffered crater counting, *Icarus*, *195*(1), 61–89, doi:10.1016/j.icarus.2007.12.009.

Grimm, R. E., and D. E. Stillman (2008), On the origin of widespread subsurface radar attenuation at Mars, *Lunar Planet. Sci.*, *XXXIX*, Abstract 2251.

Head, J. W., and S. Pratt (2001), Extensive Hesperian-aged south polar ice sheet on Mars: Evidence for massive melting and retreat, and lateral flow and ponding of meltwater, *J. Geophys. Res.*, *106*(E6), 12,275–12,299, doi:10.1029/2000JE001359.

Head, J. W., and R. Roth (1976), Mars pedestal crater escarpments: Evidence for ejecta-related emplacement, paper presented at Symposium on Planetary Cratering Mechanics, U.S. Geol. Surv., Flagstaff, Ariz.

Head, J. W., J. F. Mustard, M. A. Kreslavsky, R. E. Milliken, and D. R. Marchant (2003), Recent ice ages on Mars, *Nature*, *426*, 797–802, doi:10.1038/nature02114.

Head, J. W., D. R. Marchant, M. C. Agnew, C. I. Fassett, and M. A. Kreslavsky (2006), Extensive valley glacier deposits in the northern mid-latitudes of Mars: Evidence for Late Amazonian obliquity-driven climate change, *Earth Planet. Sci. Lett.*, *241*, 663–671, doi:10.1016/j.epsl.2005.11.016.

Herrick, R. R., and K. K. Hessen (2006), The planforms of low-angle impact craters in the northern hemisphere of Mars, *Meteorit. Planet. Sci.*, *41*(10), 1483–1495, doi:10.1111/j.1945-5100.2006.tb00431.x.

Holt, J. W., M. E. Peters, S. D. Kempf, D. L. Morse, and D. D. Blankenship (2006), Echo source discrimination in single-pass airborne radar sounding data from the Dry Valleys, Antarctica: Implications for orbital sounding of Mars, *J. Geophys. Res.*, *111*, E06S24, doi:10.1029/2005JE002525.

Holt, J. W., et al. (2008), Radar sounding evidence for buried glaciers in the southern mid-latitudes of Mars, *Science*, *322*, 1235–1238, doi:10.1126/science.1164246.

Jaumann, R., et al. (2007), The High-Resolution Stereo Camera (HRSC) experiment on Mars Express: Instrument aspects and experiment conduct from interplanetary cruise through the nominal mission, *Planet. Space Sci.*, *55*(7–8), 928–952, doi:10.1016/j.pss.2006.12.003.

Kadish, S. J., and N. G. Barlow (2006), Pedestal crater distribution and implications for a new model of formation, *Proc. Lunar Planet. Sci. Conf.*, *XXXVII*, Abstract 1254.

Kadish, S. J., J. W. Head, N. G. Barlow, and D. R. Marchant (2008), Martian pedestal craters: Marginal sublimation pits implicate a climate-related formation mechanism, *Geophys. Res. Lett.*, *35*, L16104, doi:10.1029/2008GL034990.

Kadish, S. J., N. G. Barlow, and J. W. Head (2009), Latitude dependence of Martian pedestal craters: Evidence for a sublimation-driven formation mechanism, *J. Geophys. Res.*, *114*, E10001, doi:10.1029/2008JE003318.

Kadish, S. J., J. W. Head, and N. G. Barlow (2010), Pedestal crater heights on Mars: A proxy for the thicknesses of past, ice-rich, Amazonian deposits, *Icarus*, *210*, 92–101, doi:10.1016/j.icarus.2010.06.021.

Laskar, J., B. Levrard, and J. F. Mustard (2002), Orbital forcing of the Martian polar layered deposits, *Nature*, *419*, 375–377, doi:10.1038/nature01066.

Laskar, J., A. C. M. Correia, M. Gastineau, F. Joutel, B. Levrard, and P. Robutel (2004), Long term evolution and chaotic diffusion of the insolation quantities of Mars, *Icarus*, *170*, 343–364, doi:10.1016/j.icarus.2004.04.005.

Leonard, G. J., and K. L. Tanaka (2001), Geologic map of the Hellas region of Mars, scale 1:5,000,000, *U.S. Geol. Surv. Map, I-2694*.

Leuschen, C., S. Clifford, and P. Gogineni (2003), Simulation of a surface-penetrating radar for Mars exploration, *J. Geophys. Res.*, *108*(E4), 8035, doi:10.1029/2002JE001875.

Levy, J. S., D. R. Marchant, and J. W. Head (2010), Thermal contraction crack polygons on Mars: A synthesis from HiRISE, Phoenix, and terrestrial analog studies, *Icarus*, *206*(1), 229–252, doi:10.1016/j.icarus.2009.09.005.

Matzler, C. (1998), Microwave properties of ice and snow, in *Solar System Ices*, edited by B. Schmitt et al., pp. 241–257, Kluwer Acad., Dordrecht, Netherlands.

McCauley, J. F. (1973), Mariner 9 evidence for wind erosion in the equatorial and mid-latitude regions of Mars, *J. Geophys. Res.*, *78*(20), 4123–4137, doi:10.1029/JB078i020p04123.

McKeown, N. K., J. L. Bishop, E. Z. Noe Dobrea, B. L. Ehlmann, M. Parente, J. F. Mustard, S. L. Murchie, G. A. Swayze, J.-P. Bibring, and E. A. Silver (2009), Characterization of phyllosilicates observed in the central Mawrth Vallis region, Mars, their potential formational processes, and implications for past climate, *J. Geophys. Res.*, *114*, E00D10, doi:10.1029/2008JE003301.

Mellon, M. T., and B. M. Jakosky (1995), The distribution and behavior of Martian ground ice during past and present epochs, *J. Geophys. Res.*, *100*(E6), 11,781–11,799, doi:10.1029/95JE01027. (Correction to "The distribution and behavior of Martian ground ice during past and present epochs" by Michael T. Mellon and Bruce M. Jakosky, *J. Geophys. Res.*, *100*(E11), 23,367–23,370, doi:10.1029/95JE03310, 1995.)

Mellon, M. T., M. C. Malin, R. E. Arvidson, M. L. Searls, H. G. Sizemore, T. L. Heet, M. T. Lemmon, H. U. Keller, and J. Marshall (2009), The periglacial landscape at the Phoenix landing site, *J. Geophys. Res.*, *114*, E00E06, doi:10.1029/2009JE003418.

Mouginot, J., W. Kofman, A. Safaeinili, C. Grima, A. Herique, and J. J. Plaut (2009), MARSIS surface reflectivity of the south residual cap of Mars, *Icarus*, *201*(2), 454–459, doi:10.1016/j.icarus.2009.01.009.

Muhleman, D. O., B. J. Butler, A. W. Grossman, and M. A. Slade (1991), Radar Images of Mars, *Science*, *253*, 1508–1513, doi:10.1126/science.253.5027.1508.

Muhleman, D. O., A. W. Grossman, and B. J. Butler (1995), Radar investigations of Mars, Mercury, and Titan, *Annu. Rev. Earth Planet. Sci.*, *23*, 337–374, doi:10.1146/annurev.ea.23.050195.002005.

Murchie, S., et al. (2007), Compact Reconnaissance Imaging Spectrometer for Mars (CRISM) on Mars Reconnaissance Orbiter (MRO), *J. Geophys. Res.*, *112*, E05S03, doi:10.1029/2006JE002682.

Murray, B. C., L. A. Soderblom, J. A. Cutts, R. P. Sharp, D. J. Milton, and R. B. Leighton (1972), Geological framework of the south polar region of Mars, *Icarus*, *17*(2), 328–345, doi:10.1016/0019-1035(72)90004-8.

Mustard, J. F., C. D. Cooper, and M. K. Rifkin (2001), Evidence for recent climate change on Mars from the identification of youthful near-surface ground ice, *Nature*, *412*(6845), 411–414, doi:10.1038/35086515.

Mutch, P., and A. Woronow (1980), Martian rampart and pedestal craters' ejecta-emplacement: Coprates quadrangle, *Icarus*, *41*(2), 259–268, doi:10.1016/0019-1035(80)90009-3.

Nunes, D. C., and R. J. Phillips (2006), Radar subsurface mapping of the polar layered deposits on Mars, *J. Geophys. Res.*, *111*, E06S21, doi:10.1029/2005JE002609.

Nunes, D. C., S. E. Smrekar, A. Safaeinili, J. Holt, R. J. Phillips, R. Seu, and B. Campbell (2010), Examination of gully sites on Mars with the shallow radar, *J. Geophys. Res.*, *115*, E10004, doi:10.1029/2009JE003509.

Olhoeft, G. R., and D. W. Strangway (1975), Dielectric properties of the first 100 meters of the Moon, *Earth Planet. Sci. Lett.*, *24*, 394–404, doi:10.1016/0012-821X(75)90146-6.

Pelkey, S. M., et al. (2007), CRISM multispectral summary products: Parameterizing mineral diversity on Mars from reflectance, *J. Geophys. Res.*, *112*, E08S14, doi:10.1029/2006JE002831.

Pettinelli, E., G. Vannaroni, A. Cereti, F. Paolucci, G. D. Monica, M. Storini, and F. Bella (2003), Frequency and time domain permittivity measurements on solid CO_2 and solid CO_2-soil mixtures as Martian soil simulants, *J. Geophys. Res.*, *108*(E4), 8029, doi:10.1029/2002JE001869.

Phillips, R. J., et al. (1973), The Apollo 17 Lunar Sounder, *Proc. Lunar Planet. Sci. Conf.*, *4*, 2821–2831.

Phillips, R. J., et al. (2008), Mars north polar deposits: Stratigraphy, age, and geodynamical response, *Science*, *320*(5880), 1182–1185, doi:10.1126/science.1157546.

Picardi, G., et al. (2004), Performance and surface scattering models for the Mars Advanced Radar for Subsurface and Ionospheric Sounding (MARSIS), *Planet. Space Sci.*, *52*, 149–156, doi:10.1016/j.pss.2003.08.020.

Picardi, G., et al. (2005), Radar sounding of the subsurface of Mars, *Science*, *310*, 1925–1928, doi:10.1126/science.1122165.

Plaut, J. J., R. Kahn, E. A. Guinness, and R. E. Arvidson (1988), Accumulation of sedimentary debris in the south polar region of Mars and implications for climate history, *Icarus*, *76*(2), 357–377, doi:10.1016/0019-1035(88)90076-0.

Plaut, J. J., A. Safaeinili, J. W. Holt, R. J. Phillips, J. W. Head, R. Seu, N. E. Putzig, and A. Frigeri (2009), Radar evidence for ice in lobate debris aprons in the mid-northern latitudes of Mars, *Geophys. Res. Lett.*, *36*, L02203, doi:10.1029/2008GL036379.

Poulet, F., J. P. Bibring, J. F. Mustard, A. Gendrin, N. Mangold, Y. Langevin, R. E. Arvidson, B. Gondet, and C. Gomez (2005), Phyllosilicates on Mars and implications for early Martian climate, *Nature*, *438*(7068), 623–627, doi:10.1038/nature04274.

Scott, D. H., and K. L. Tanaka (1986), Geologic map of the western equatorial regions of Mars, scale 1:15,000,000, *U.S. Geol. Surv. Map, I-1802-A*.

Seu, R., D. Biccari, L. V. Lorenzoni, R. J. Phillips, L. Marinangeli, G. Picardi, A. Masdea, and E. Zampolini (2004), SHARAD: The MRO 2005 shallow radar, *Planet. Space Sci.*, *52*, 157–166, doi:10.1016/j.pss.2003.08.024.

Seu, R., et al. (2007), SHARAD sounding radar on the Mars Reconnaissance Orbiter, *J. Geophys. Res.*, *112*, E05S05, doi:10.1029/2006JE002745.

Sharp, R. P., and M. C. Malin (1975), Channels on Mars, *Geol. Soc. Am. Bull.*, *86*(5), 593–609, doi:10.1130/0016-7606(1975)86<593:COM>2.0.CO;2.

Skinner, J. A., T. M. Hare, and K. L. Tanaka (2006a), Digital renovation of the atlas of Mars 1:15,000,000-scale global geologic series maps, *Lunar Planet. Sci.*, *XXXVII*, Abstract 2331.

Skinner, J. A., T. M. Hare, and K. L. Tanaka (2006b), Northern plains craterforms: Evidence for the accumulation and degradation of paleomantles, *Lunar Planet. Sci.*, *XXXVII*, Abstract 1476.

Smith, D. E., et al. (2001), Mars Orbiter Laser Altimeter: Experiment summary after the first year of global mapping of Mars, *J. Geophys. Res.*, *106*(E10), 23,689–23,722, doi:10.1029/2000JE001364.

Smith, I. B., and J. W. Holt (2010), Onset and migration of spiral troughs on Mars revealed by orbital radar, *Nature*, *465*(7297), 450–453, doi:10.1038/nature09049.

Soderblom, L. A., T. J. Kreidler, and H. Masursky (1973), Latitudinal distribution of a debris mantle on the Martian surface, *J. Geophys. Res.*, *78*(20), 4117–4122, doi:10.1029/JB078i020p04117.

Squyres, S. W. (1979), The Distribution of Lobate Debris Aprons and Similar Flows on Mars, *J. Geophys. Res.*, *84*(B14), 8087–8096, doi:10.1029/JB084iB14p08087.

Stillman, D., and G. Olhoeft (2008), Frequency and temperature dependence in electromagnetic properties of Martian analog minerals, *J. Geophys. Res.*, *113*, E09005, doi:10.1029/2007JE002977.

Tanaka, K. L., and E. J. Kolb (2001), Geologic history of the polar regions of Mars based on Mars Global Surveyor data, *Icarus*, *154*, 3–21, doi:10.1006/icar.2001.6675.

Tanaka, K. L., and D. H. Scott (1987), Geologic map of the polar regions of Mars, *U.S. Geol. Surv. Map, I-1802-C*.

Thomas, P. C., M. C. Malin, K. S. Edgett, M. H. Carr, W. K. Hartmann, A. P. Ingersoll, P. B. James, L. A. Soderblom, J. Veverka, and R. Sullivan (2000), North-south geological differences between the residual polar caps on Mars, *Nature*, *404*, 161–164, doi:10.1038/35004528.

Ulaby, F. T., R. K. Moore, and A. K. Fung (1986), *Microwave Remote Sensing: Active and Passive*, Artech, Norwood, Mass.

Wait, J. R. (1970), *Electromagnetic Waves on Stratified Media*, 2nd ed., Pergamon, New York.

Ward, S. H., G. R. Jiracek, and W. I. Linlor (1968), Electromagnetic reflection from a plane-layered lunar model, *J. Geophys. Res.*, *73*(4), 1355–1372, doi:10.1029/JB073i004p01355.

Watters, T. R., et al. (2007), Radar sounding of the Medusae Fossae Formation Mars: Equatorial ice or dry, low-density deposits?, *Science*, *318*(5853), 1125–1128, doi:10.1126/science.1148112.

Williams, D. A., et al. (2009), The Circum-Hellas volcanic province, Mars: Overview, *Planet. Space Sci.*, *57*(8–9), 895–916, doi:10.1016/j.pss.2008.08.010.

Zurek, R. W., and S. E. Smrekar (2007), An overview of the Mars Reconnaissance Orbiter (MRO) science mission, *J. Geophys. Res.*, *112*, E05S01, doi:10.1029/2006JE002701.

B. Fisher, Division of Engineering, Brown University, Box D, 182 Hope St., Providence, RI 02912, USA.

J. W. Head and S. J. Kadish, Department of Geological Sciences, Brown University, 324 Brook St., Box 1846, Providence, RI 02912, USA.

J. W. Holt, University of Texas at Austin Institute for Geophysics, J.J. Pickle Research Campus, Bldg. 196, 10100 Burnet Rd., Austin, TX 78758-4445, USA.

D. C. Nunes, J. J. Plaut, and S. E. Smrekar, Jet Propulsion Laboratory, California Institute of Technology, 4800 Oak Grove Dr., M/S 183-301, Pasadena, CA 91101, USA. (Daniel.Nunes@jpl.nasa.gov)

R. J. Phillips, Planetary Sciences, Southwest Research Institute, 1050 Walnut St., Boulder, CO 80302, USA.